Summer 8-15-2018

In Vivo Vascular Imaging with Photoacoustic Microscopy

Hsun-Chia Hsu
Washington University in St. Louis

WASHINGTON UNIVERSITY IN ST. LOUIS

School of Engineering and Applied Science
Department of Biomedical Engineering

Dissertation Examination Committee:
Lihong V. Wang, Co-Chair
Mark A. Anastasio, Co-Chair
Jin-Moo Lee
Jung-Tsung Shen
Lan Yang

In Vivo Vascular Imaging with Photoacoustic Microscopy

by
Hsun-Chia Hsu

A dissertation presented to
The Graduate School
of Washington University in
partial fulfillment of the
requirements for the degree
of Doctor of Philosophy

August 2018
St. Louis, Missouri

Table of Contents

List of Figures

List of Tables

Acknowledgements

I would like to express my sincere thanks to my advisor, Prof. Lihong V. Wang, for his support and guidance throughout my Ph.D. journey. The Wang lab has helped me learn the way to perform first-rate research, to understand the importance of a positive and persistent attitude, and to experience the significance of solving vital medical/scientific problems. I also appreciate the generous help of many of my lab colleagues, including Junjie Yao, Terence Tsz Wai Wong, Lei Li, Lidai Wang, Junhui Shi, Yang Li, Toru Imai, Wen Bao, and Konstantin Maslov. Without their inspiration and support, my work could not have been accomplished smoothly.

I am thankful to my committee members and collaborating faculty, Profs. Mark Anastasio, Jin-Moo Lee, Lan Yang, and Jung-Tsung Shen. Especially, I thank Drs. Jin-Moo Lee and Andria Ford for their patience and help with my medical project. I am also most grateful to Dr. Mark Anastasio for his wise advice throughout the progress of my thesis, and I thank Drs. Jung-Tsung Shen and Lan Yang for their valuable advice and support.

Last, but definitely not least, I owe special thanks to my friends, family, and girl friend for their boundless love, encouragement, and unconditional support, all of which have made this dissertation possible and the whole process rewarding.

Hsun-Chia Hsu

Caltech

August 2018

Dedicated to my family and girl friend

ABSTRACT OF THE DISSERTATION

In Vivo Vascular Imaging with Photoacoustic Microscopy

by

Hsun-Chia Hsu

Doctor of Philosophy in Biomedical Engineering

Washington University in St. Louis, 2018

Professor Lihong V. Wang, Co-Chair

Professor Mark A. Anastasio, Co-Chair

Photoacoustic (PA) tomography (PAT) has received extensive attention in the last decade for its capability to provide label-free structural and functional imaging in biological tissue with highly scalable spatial resolution and penetration depth. Compared to modern optical modalities, PAT offers speckle-free images and is more sensitive to optical absorption contrast (with 100% relative sensitivity). By implementing different regimes of optical wavelength, PAT can be used to image diverse light-absorbing biomolecules. For example, hemoglobin is of particular interest in the visible wavelength regime owing to its dominant absorption, and lipids and water are more commonly studied in the near-infrared regime.

In this dissertation, one challenge was to quantitatively investigate red-blood-cell dynamics in nailfold capillaries with single-cell resolution PA microscopy (PAM). We recruited healthy volunteers and measured multiple hemodynamic parameters based on individual red blood cells (RBCs). Statistical analysis revealed the process of oxygen release and changes in flow speed for RBCs in a capillary. For the first time on record, oxygen release from individual RBCs in human capillaries was imaged with nearly real-time speed, and the work paved the way for our following study of a specific blood disorder.

We next conducted a pilot study on sickle cell disease (SCD), measuring and comparing the parameters related to RBC dynamics between healthy subjects and patients with SCD. In the patient group, we found that capillaries tended to be more tortuous, dilated, and had higher number density. In addition, abnormal RBCs tended to have lower oxygenation in the inlet of a capillary, from where they flowed slower and released a larger fraction of oxygen than normal RBCs. As the only imaging modality able to observe the real-time dynamics of the oxygen release of individual RBCs, PAM provides medically valuable information for diagnostic purposes.

As the last focus of this dissertation, we tackled the limited view problem in PAM by introducing an off-axis illumination technique for complementing the original detection view. We demonstrated this technique numerically and then experimentally on phantoms and animals. This simple but very effective method revealed abundant vertical vasculature in a mouse brain that had long been missed by conventional top-illumination PAM. This technique greatly advances future studies on neurovascular responses in mouse brains.

Chapter 1 Introduction

This chapter introduces photoacoustic tomography (PAT), which consists of photoacoustic microscopy (PAM) and photoacoustic computed tomography (PACT). In section 1.1, the physical mechanism of the photoacoustic (PA) effect is reviewed, followed by an introduction to several representative implementations of PAT. The motivations for studying *in vivo* vascular imaging with PAM are discussed in the next section.

1.1 Introduction to Photoacoustic Tomography

The photoacoustic effect, the foundation of PAT, is a physical phenomenon in which energy is converted by materials upon excitation by short light pulses (typically on the order of 10 ns).[1] When an optical pulse is absorbed by the materials, part of the optical energy is converted into heat through non-radiative relaxation. The heated region undergoes thermoelastic expansion, which results in further energy conversion from heat to acoustic energy in the form of propagating ultrasonic waves (PA waves). In tissue, ultrasonic waves have a scattering coefficient that is 2 – 3 orders of magnitude smaller than that of optical waves. Therefore, PAT can penetrate much deeper than the transport mean free path of photons (~ 1 mm), up to several centimeters deep. Moreover, PAT provides highly scalable imaging resolution and penetration depth at ultrasonic frequencies, making PAT currently the only imaging modality that can span broad length-scales, from subcellular organelles to organs.[2]

PAT can be categorized into PAM and PACT, based on the image formation methods. In PAM, the optical excitation and acoustic detection are confocally aligned in order to maximize

the sensitivity, and a three-dimensional (3D) volumetric image is formed by raster scanning, achieved by moving either the imaging module's focus or the imaged samples. The lateral resolution of PAM depends on the optical or acoustic confinement in the lateral direction, whichever is finer. In the axial direction, the resolution is determined by bandwidth of the ultrasonic transducer.[3]

In PACT, PA signals are collected at multiple locations around the object illuminated by unfocused light. The image is then reconstructed from the PA signals by using the inverse spherical Radon transformation.[4] Modern PACT systems commonly use spherical,[5,6] ring-shape,[7,8] or planar detection geometry.[9,10] For more accurate reconstruction, mechanical scanning is often employed to achieve denser sampling. The spatial resolutions of PACT depend positively on the central frequency and bandwidth of the ultrasonic transducer array. However, improvements in these parameters compromise the penetration depth and the effective focal zone accordingly.

In both PAM and PACT, the amplitude of the initial PA pressure is proportional to the optical absorption coefficient of the absorber in units of cm^{-1}, to the non-radiative quantum yield, and to the local optical fluence (or exposure) in units of J/m^2. Environment parameters such as temperature[11] and pH value[12] also influence PA signal amplitude.

1.2 Motivation

In 2017, the American Heart Association reported that, between 2011 and 2014, 92.1 million American adults (>1 in 3) had ≥1 type of cardiovascular disease. This number is estimated to increase to 43.9% of the US population by 2030,[13] so it is increasingly crucial to devote more

efforts to developing effective diagnostic tools and treatments. In this regard, PAT, with the advantages of multi-scale imaging and 100% sensitivity to optical absorption, has proven to be a powerful imaging modality for blood imaging in the past decade.[14–19] This dissertation focuses on advances in *in vivo* vascular imaging with PAM.

Chapter 2 introduces our research on *in vivo* monitoring of nailfold capillary hemodynamics with single-cell resolution PAM. Wide field mages were captured to reveal the morphology of capillaries in this area. In addition, time-lapse dynamics of RBCs within individual capillaries were recorded with a high-speed zoom-in mode. Further analyses were done to determine the dynamics of oxygen release from red blood cells (RBCs) flowing through capillaries.

Chapter 3 extends the work in Chapter 2 to an investigation of sickle cell disease, an inherited blood disorder often found in people of African descent. Wide-field and time-lapse images were acquired and then compared between control and patient groups. Results from PAM were also correlated with clinical data from blood tests and MRI.

Chapter 4 presents an interesting technique for augmenting the detection view of PAM. Conventional top-illumination PAM, with a top transducer collinearly aligned with the illumination beam, can barely detect PA signals from vertical structures, due to the boundary build-up property of PA signals. In this work, an oblique illumination was introduced to reduce the dimensions of the confocal region so that vertical structures become detectable. This technique allows PAM to image complete vasculature down to 1 mm in depth.

Chapter 5 summarizes all the findings from the different chapters and outlines prospective directions for each research area.

Chapter 2 *In vivo* photoacoustic microscopy of human cuticle microvasculature with single-cell resolution

As a window on the microcirculation, human cuticle capillaries provide rich information about the microvasculature, such as its morphology, density, dimensions or even blood flow speed. Many imaging technologies have been employed to image human cuticle microvasculature. However, almost none of these techniques can non-invasively observe the process of oxygen release from single red blood cells (RBCs), an observation which can be used to study healthy tissue functionalities or to diagnose, stage, or monitor diseases. In this study, for the first time, we adapted single-cell resolution photoacoustic microscopy (photoacoustic flowoxigraphy) to image cuticle capillaries and quantified multiple functional parameters. Our results show more oxygen release in the curved cuticle tip region than in other regions of a cuticle capillary loop, associated with a low of RBC flow speed in the tip region. Further analysis suggests that in addition to the RBC flow speed, other factors, such as the drop of the partial oxygen pressure in the tip region, drive RBCs to release more oxygen in the tip region.

2.1 Background

The microcirculation comprises microvascular networks of arterioles, capillaries, and venules, which are fundamental for thermoregulation and for transporting nutrients and gases to maintain the metabolism of cells.[20] However under disease states such as severe hemorrhage, cardiogenic

shock, sepsis,[20,21] and systemic scleroderma,[22–24] the associated dysfunction of the microcirculation may cause heterogeneous hypoxia, impairing cell functioning in tissues and even causing multiple organ failures.[20,21] In other cases, hypertension and diabetes mellitus can cause microvascular complications such as microvessel rarefaction and retinopathy, respectively.[25,26] Tumors will often induce angiogenesis of the microvascular system in their microenvironment.[27] To better understand the fundamental mechanisms of these diseases, diagnose them in early stages, and evaluate the effectiveness of various therapies, it is essential to develop tools to monitor important microvascular parameters of blood perfusion. These parameters include function capillary density (which is defined as the total length of capillaries perfused by red blood cells per observed area in units of cm^{-1}),[20] total hemoglobin concentration (C_{Hb}), the oxygen saturation of blood (sO_2), the directional derivative of sO_2 along the blood flow direction ($D sO_2$), and the speed of blood flow (v_{Hb}).[28]

Primary medical imaging modalities, such as single photon emission computed tomography, functional magnetic resonant imaging, positron emission tomography, ultrasonography, and diffuse optical tomography, have been used for years to image cardiovascular or cerebral blood flow.[29–33] Additionally, contrast-enhanced ultrasonography, which detects nonlinear oscillation of microbubbles (only a few microns in size) under low mechanical index conditions, has been applied to imaging blood perfusion around focal liver lesions and the renal cortex.[34–36] Even though these techniques are the best we have to date to image blood flows in organs deep in the body, they are limited by their millimeter-size resolution. Thus, these modalities are not efficient in monitoring microcirculation, which in general contains vessels smaller than 100 microns.[20]

As an alternative, the cutaneous and sublingual microcirculations have been proposed as a representative model visceral microcirculation because they are accessible by optical-based

imaging techniques, which provide higher resolution than most other imaging modalitie.[37–39] Patients with chronic diseases such as hypertension, renal disease, and coronary artery disease have been observed to have distinct cutaneous microvascular parameters.[25,40,41] Monitoring cutaneous microvascular functioning provides valuable information for evaluating peripheral microvascular diseases, such as Raynaud's disease and peripheral arterial disease.[23,42,43] To this end, optical scattering-based techniques, such as laser Doppler imaging,[41,44] near-infrared spectroscopy[45,46] and reflectance spectroscopy[47,48] are used to detect scattered light from tissues. Over a sub-millimeter sampling volume, laser Doppler imaging can measure the average speed of flow, and near-infrared spectroscopy and reflectance spectroscopy can measure both the average flow speed and the oxygen saturation. On the wide-field scale, nailfold videomicroscopy,[23,49,50] orthogonal polarization spectral imaging,[51,52] sidestream dark field imaging,[53] and optical coherent tomography[54,55] can provide wide-field information about function capillary density and the speed of flow with lateral resolutions ranging from sub-microns to around 15 microns, which covers from the thinnest capillaries to the wider arterioles and venules. The imaging depth can go as deep as 400 microns for nailfold videomicroscopy and around 1-3 mm for optical-based techniques. Combined with an endoscope, these modalities can image the gastric or intestinal microcirculation with a tolerable compromise of image quality. However, none of these imaging modalities can provide sO_2 and v_{Hb} information at the same time.

In the recent years, optical resolution photoacoustic microscopy (OR-PAM) has shown promise in in vivo microvascular imaging, with its ability to provide wide-field, capillary-resolving, and hemoglobin-sensitive images.[10,56–70] Combined with the flow speed imaging techniques reported previously,[17,71,72] OR-PAM has been demonstrated as a powerful tool to acquire such important

parameters of the microcirculation as sO_2, DsO_2, C_{Hb}, v_{Hb}, and the metabolic rate of oxygen in tissues.[73,74] In this study, we implemented dual-wavelength in vivo OR-PAM for investigating oxygen release in cuticle capillaries. This is the first time that oxygen release dynamics in human cuticle capillaries has been monitored. The correlation between oxygen releases and the speed of RBCs and between oxygen release and the first-order time-derivative of sO_2 have also been analyzed in a cuticle capillary. The spatial- and time-resolved information acquired by OR-PAM may help in early-stage diagnosis of perivascular diseases, such as Raynaud's syndrome, and in diagnosing heterogeneous microcirculation of interior organs.

2.2 Methods

2.2.1 Experimental protocol

Nine healthy consenting volunteers (with ages ranging from 23 to 30, seven males, two females) were recruited with consents in this study. For each volunteer, we imaged the cuticle capillaries in the fourth finger (the ring finger) of the left hand.[55] Before each experiment, the volunteer rested in the temperature-controlled laboratory (at 20°C) for 15 minutes to adapt to the environmental temperature, since nailfold microcirculation is known to be sensitive to the surrounding temperature. The imaged area was then cleaned with alcohol swabs, and the hand was comfortably put on a homemade hand mount, without occlusion of blood flow, as shown in Fig. 2.1. During the data acquisition period, the photoacoustic (PA) scanning head was scanned over a single cuticle capillary at a time for three-dimensional imaging, with a 10 Hz C-scan rate (high-speed scanning mode) for about 40 seconds. At least three cuticle capillaries were recorded for each volunteer. The total experimental time spent on a volunteer was less than 1.5 hours,

including rests every 20 minutes to prevent numbness of the extremities. The human study was approved by the Institutional Review Board of Washington University in St. Louis, and the pulse energies of the excitation lasers used in each experiment were within the ANSI laser safety limit (20 mJ·cm-2).

2.2.2 System setup

In order to monitor the real-time microcirculation of a single cuticle, dual-wavelength excitation at 532 nm (SPOT, Elforlight, Northants, UK) and 559 nm (INNOSLAB, Edgewave, Würselen, Germany) was implemented on a high-speed voice-coil scanning PA microscope,[75] shown in Figure 1. The two short-pulse (< 10 ns) excitation beams, with a 10-μs temporal delay between them, were first attenuated, combined, and passed through an optical spatial filter made of a spherical lens and a pinhole (50 μm in diameter, P50C, Thorlabs, NJ, USA), then they were guided into a customized photonic crystal fiber (Thorlabs, NJ, USA). The other end of the fiber was connected to the scanning PA probe. The output beams from the fiber were focused by a lens pair with a numerical aperture (N.A.) of 0.1 in water, and were reflected by an acoustic-optical beam combiner, made of two right-angle prisms sandwiching a coated aluminum layer on the hypotenuse faces. The emitted PA signals in the reflection direction were collected by an acoustic lens and then detected by a 50-MHz ultrasonic transducer (V214, Olympus NDT, PA, USA). The received PA signals were amplified (ZFL-500LN+, Mini-circuits, NY, USA), filtered and then digitized by a DAQ system (ATS9350, Alazar Tech. Inc., QC, Canada). The optical focusing and the bandwidth of the transducer provided 3-μm lateral resolution and 15-μm axial resolution, respectively. In order to compensate for variations of the optical energy, pulse by pulse, a photodiode was set up after the optical spatial filter. The laser pulse energy on the

sample surface was between 35 nJ and 50 nJ in high-speed mode with the laser repetition rate of 20 kHz.

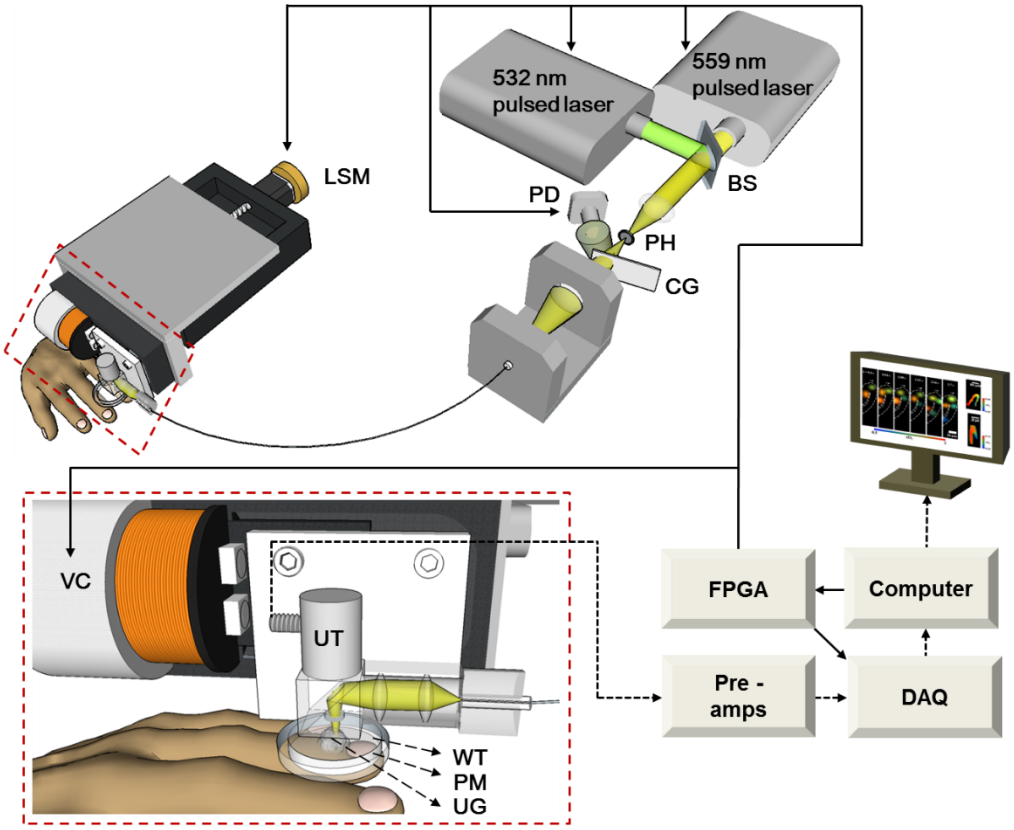

Figure 2.1 Schematic of the single-cell OR-PAM system. BS, beam splitter; CG, coverglass; LSM, linear step motor; PD, photodiode; PH, pin hole; PM, plastic membrane; UG, ultrasound gel; UT, ultrasound transducer; VC, voice coil motor; WT, water.

During single cuticle capillary imaging, the PA probe mounted on the voice coil motor was driven to scan linearly with 100 Hz (B-scan) frequency within a 250-μm range. Combined with an additional linear translational stage (PLS-85, PI miCos, Eschbach, Germany), the system was set to repeatedly acquire 250 μm × 40 μm C-scan images at 10 Hz. The lasers, photodiode, and DAQ system were synchronously triggered at 20 kHz by a programmed field-programmable gate array card (FPGA) (PCI-7830R, National Instruments, TX, USA). This dual-wavelength high-

speed PA microscopy has been previously demonstrated for measuring sO_2 and blood flow speed in mouse capillaries.[75]

2.2.3 Principle of sO_2 measurement

After C-scan images have been acquired with two wavelengths, the sO_2 values can be calculated pixel-by-pixel according to the method described in references.[76,77] In short, the photoacoustic amplitude from a single pixel is proportional to the product of the optical absorption of the hemoglobin (oxy- or deoxy- hemoglobin) and the optical fluence at the pixel, so we have

$$\text{PA signal}(\lambda_i) = \mu_a(\lambda_i) \cdot \text{F}(\lambda) = \{\varepsilon_{HbR}(\lambda_i)[\text{HbR}] + \varepsilon_{HbO_2}(\lambda_i)[\text{HbO}_2]\} \cdot \text{F}(\lambda_i), \qquad (2.1)$$

In order to solve for [HbR] and $[\text{HbO}_2]$, two wavelengths are selected to build up two independent equations. To calibrate the sO_2 calculation, the optical properties of the tissue should be considered as well. We followed the same procedure as in reference[76] to calibrate the system. To mimic the optical properties of human tissue, the calibration was done in mouse experiments at a depth similar to that of the cuticle capillaries in human tissue.

2.3 Results

2.3.1 Monitoring of sO_2 dynamics in cuticles

Figure 2.2(a)-(b) and (c) show a top view (C-scan) and a cross-sectional view (B-scan) of the typical morphology of finger cuticle capillary loops. The acquisition time of a C-scan image was 75 seconds. The cuticle capillary loops angle toward the distal nail bed and gradually toward the epidermis. Fig. 2.2(d) shows the result of using the curvature calculated from the C-scan images

to quantitatively describe the geometric profile at different positions along the cuticles. The full-width-at-half-maximum distance is around 40 μm, which suggests that it is reasonable to define a region ±20 μm from the position with maximal curvature as the tip region of a cuticle. It is also noticeable but not surprising to observe that in most cases the tip positions (0 μm) coincide with the uppermost ends of the cuticles in the B-scan images. In Fig. 2.2(b), the insets also show pixel-by-pixel calculation of sO_2 distribution in different areas of the cuticle capillary network with different color bars. The sO_2 reduction across the tip of a cuticle capillary is within 0.2. In high-speed scanning mode, the flow and the sO_2 of single red blood cells can be resolved, as shown in the snapshots in Fig. 2.3(a) and Video 1. Fig. 2.3(b) shows the results of time-averaging over all the frames of the sO_2 image. Around the cuticle tip (the most curved position along the cuticle), an abrupt drop in sO_2 can be observed. Fig. 2.3(c) shows sO_2 versus *s*, where *s* denotes the displacement along the central axis of a cuticle capillary loop (i.e., the trace of the blood flow). The origin of *s* is coincident with the cuticle loop tip, and the RBCs flow from the negative coordinates (the upstream side of a cuticle vessel) to the positive coordinates (the downstream side). The sO_2 change with distance can be revealed more clearly by plotting the derivative of sO_2 with respect to *s*, which is defined as $DsO_2 \equiv \partial(sO_2)/\partial s$, as shown in Fig. 2.3(d). The DsO_2 values within ~ 15 μm the cuticle loop tips are approximately twice as high as those in regions 25 to 40 μm away from the tip. The paired Student's *t*-test between the tip region (yellow) and two sides (green) validates that the cuticle loop tips have significantly greater decreases in sO_2 than the sides do.

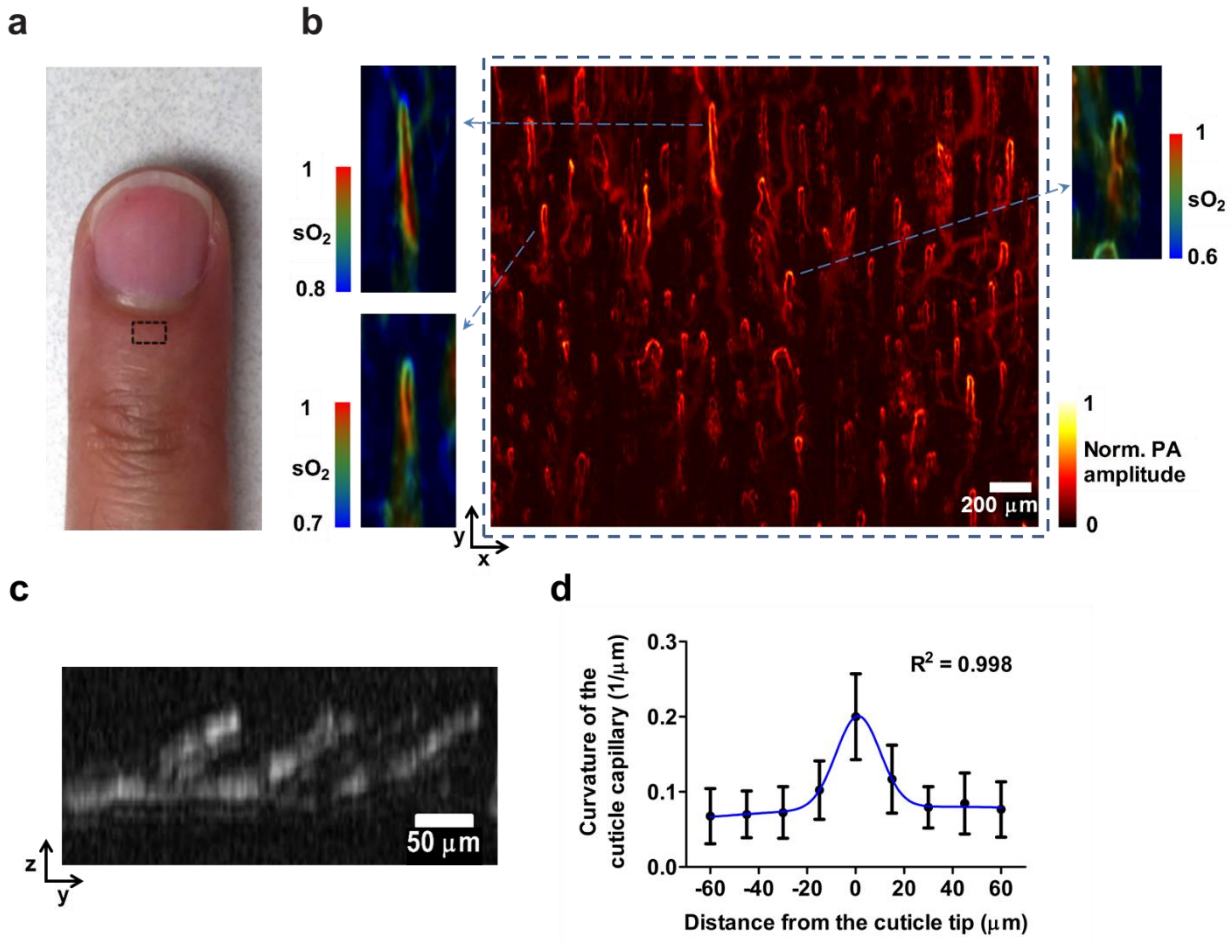

Figure 2.2 Images of finger cuticle capillaries. (**a**) Photograph of a finger with the imaged area boxed. (**b**) Wide-field PA image of cuticle capillaries shown with normalized PA amplitude. The insets show sO_2 images of selected cuticles with different color bars. (**c**) B-scan image of cuticle capillary loops. (**d**) Curvature along the cuticles (Fitting: sum of two Gaussians).

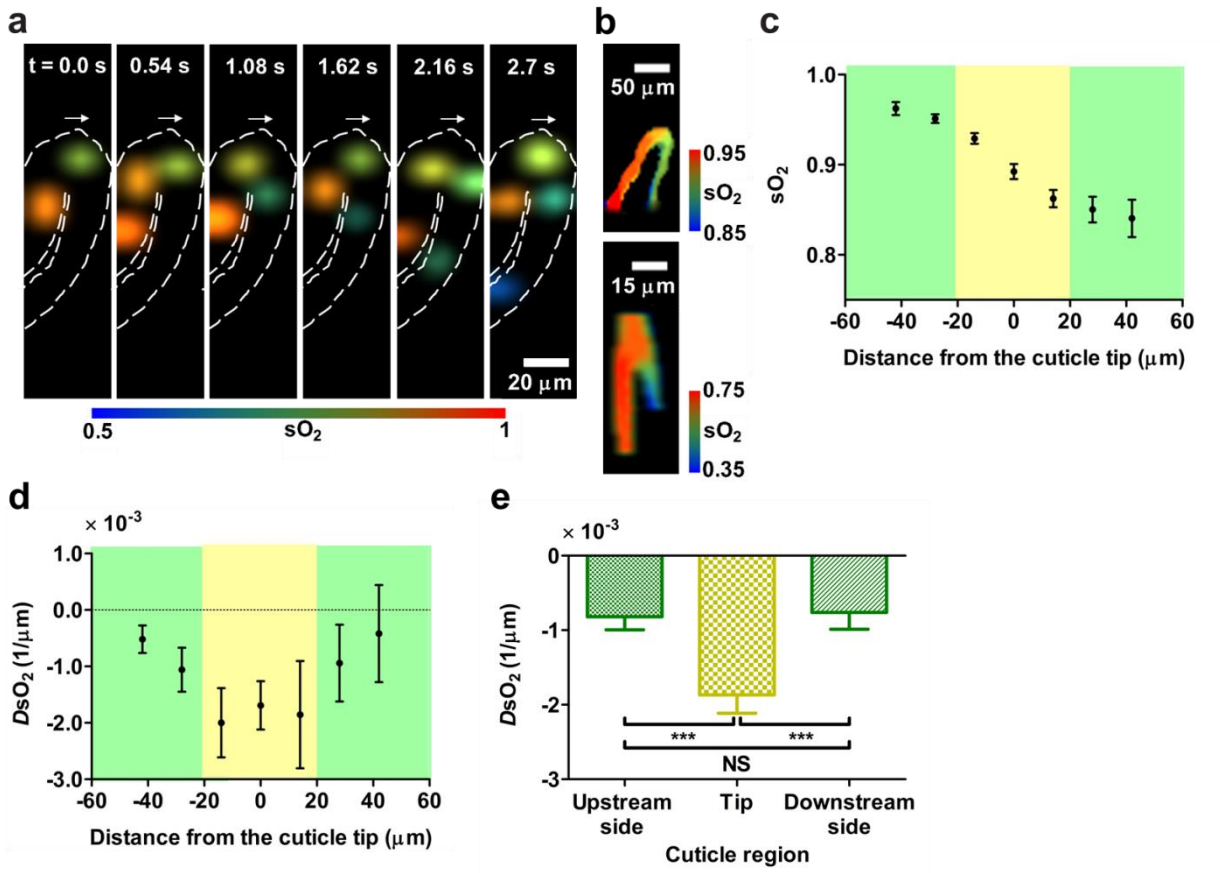

Figure 2.3 Monitoring of the single-red-blood-cell sO_2 in high-speed mode. (**a**) Selected time-lapse images of single-RBC sO_2 (Video 1) [URL: http://dx.doi.org/10.1117/1.JBO.21.5.056004]. (**b**) Time-averaged images (~10 s) of all time-lapse frames of sO_2 imaging. (**c**) Time-averaged sO_2 along the length of a cuticle capillary loop (i.e., a trace of the blood flow). (**d**) Time-averaged directional derivative of sO_2 along the length of the loops. (**e**) Statistics of (**d**): paired Student's *t*-test between the tip region (yellow) and the two side regions (green). NS: not significant ($P = 0.48$), ***$P < 0.001$, $n = 21$.

2.3.2 Measurement of RBC flow speed

By mapping the length of a curved cuticle loop s into a straight line l, Fig. 2.4(a) shows the method we used to measure the speed of RBCs flowing in cuticle capillary loops.[71] Based on Fourier analysis of the frames of a specific segment of a capillary loop acquired at different times, the longitudinal flow speeds of different segments in a cuticle can be determined by $v_{Hb} = \frac{\Delta s}{\Delta t} = \frac{\Delta l}{\Delta t} = \frac{N_t}{N_l}\frac{\Delta F_t}{\Delta F_l}$. Here, N_t and N_l are the sampled temporal and spatial lengths, and F_t and F_l are

the temporal and spatial frequencies. From Fig. 2.4(b) we can observe that the time-averaged RBC flow speed within the region of 15 μm around the cuticle tip is approximately one third lower than that in the regions between 25 μm to 40 μm away from the cuticle tip. A paired Student's *t*-test between the tip and side regions shows a significantly lower RBC flow speed around the tip region.

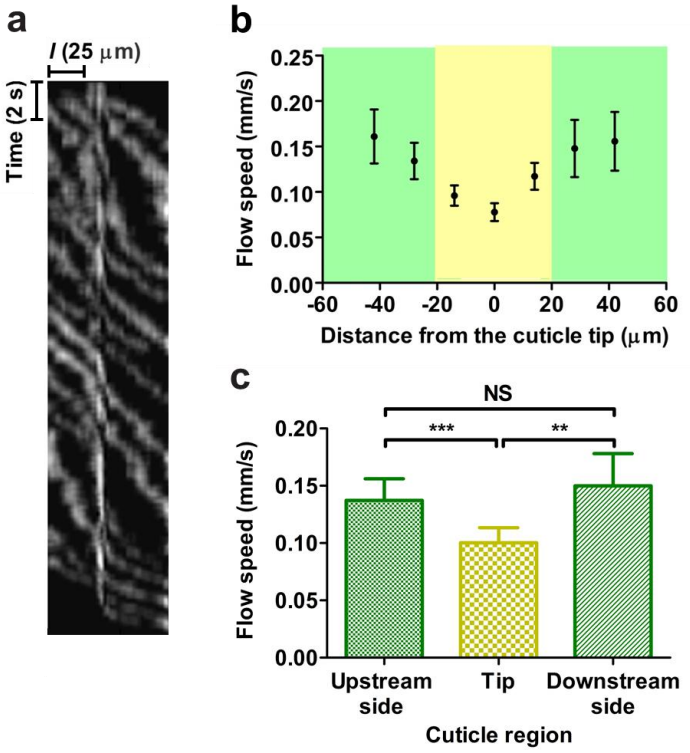

Figure 2.4 Measurement of RBC flow speed. (**a**) Image for speed measurement. (**b**) Time-averaged RBC flow speeds along the length of a cuticle loop. (**c**) Statistics of (**b**): paired Student's *t*-test between the tip region (yellow) and the two side regions (green). NS: not significant ($P = 0.45$), ***$P < 0.001$, ** $P < 0.01$, $n = 18$.

2.3.3 Measurement of hemoglobin flux in RBC flow and time derivative of sO_2

As well as imaging sO_2, we can also image the relative concentration of hemoglobin (C_{Hb}) by summing the calculated images for oxy- and deoxy-hemoglobin. To calculate the time-averaged

hemoglobin flux, we assume that the concentration and the speed are independent variables, which means that the time average of the product of the two variables is approximately equal to the product of the two time-averaged variables (in case the variances of C_{Hb} and v_{Hb} are small), so we have $\overline{\Phi_{Hb}} \approx \overline{C_{Hb}} \cdot v_{Hb,}$ where v_{Hb} is the time-averaged RBC flow speed around *x*. Fig. 2.5(a) and (c) show a nearly flat trend, and the paired *t*-tests shown in Fig. 2.5(b) and (d) suggest that the hemoglobin flux in RBC flow is approximately the same along the cuticle capillary loops: The flow of RBCs is conserved. Under steady state blood flow, $\frac{\mathrm{d}(sO_2)}{dt} = D\mathrm{sO}_2 \cdot \frac{ds}{dt}$. Similarly, we assume that both $D\mathrm{sO}_2$ and $\frac{ds}{dt}$ are independent variables, we have $\frac{\mathrm{d}(sO_2)}{dt} \approx D\mathrm{sO}_2 \cdot v_{Hb}$. The total time derivative of sO_2 along cuticle capillary loops is shown in Fig. 2.5(e). The *p* value between the upstream side and the tip is 0.03, and the *p* value between the down-stream side and the tip is 0.07, according to the paired *t*-test shown in Fig. 2.5(f).

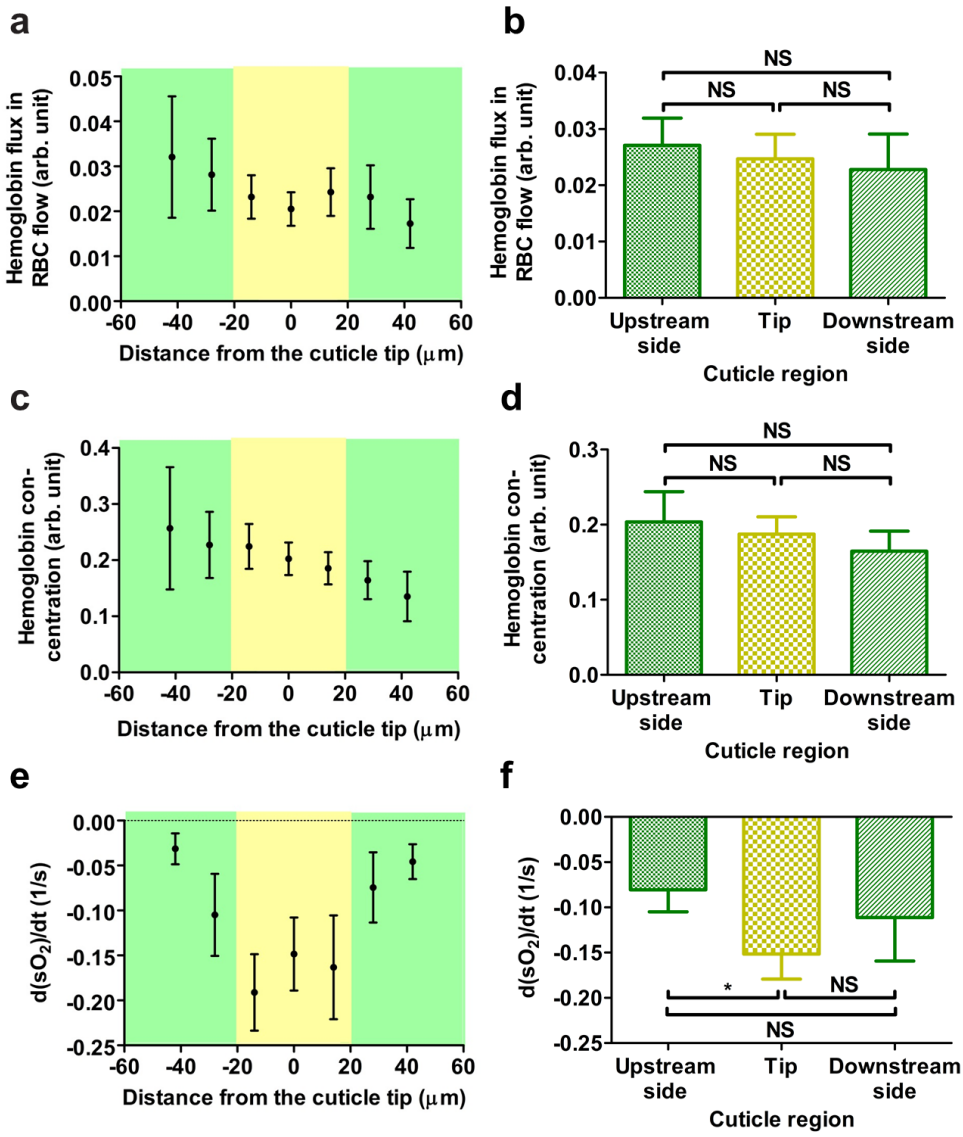

Figure 2.5 Analysis of multiple hemodynamic parameters along capillaries. (a) Time-averaged relative flow rates along the length of cuticle capillary loops. (b) Statistics of (a): paired Student's t-test between the tip region (yellow) and the two side regions (green). NS: not significant (up: P = 0.24, left: P = 0.10, right: P = 0.40), n = 13. (c) Time-averaging of hemoglobin concentration along the direction of the length of cuticles. (d) Statistics of (c): paired Student's t-test between the tip region (yellow) and the two side regions (green). NS: not significant (up: P = 0.33, left: P = 0.45, right: P = 0.21), n = 18. (e) Time-averaged values of d(sO2)/dt along the length of cuticle capillary loops. (f) Statistics of (e): paired Student's t-test between the tip region (yellow) and the two side regions (green). *P = 0.03, NS: not significant (up: P = 0.07, down: P = 0.25), n = 15.

2.4 Discussion

In this study, we demonstrated the ability of single-cell resolution OR-PAM to monitor the microcirculation in cuticle capillaries with a temporal resolution of 0.1 second. Compared to nailfold videocapillaroscopy and optical computed tomography,[55] OR-PAM can not only image the morphology, dimensions, and vessel density of cuticle capillary loops, but also measure multiple hemodynamic parameters, such as sO_2, DsO_2, C_{Hb}, and v_{Hb}. Monitoring these functional parameters at the fundamental level of the physiology of oxygen transport can potentially help biologists and physicians to understand the mechanisms of oxygen transport in the skin and to define clinical standards for early-stage diagnosis and evaluation of perivascular diseases, such as Raynaud's phenomenon and systemic scleroderma, before the capillaries undergo observable changes in morphology.

The time-averaged DsO_2 results in Fig. 2.3(d) indicate that RBCs release more oxygen in the tip region over a length of around 30 μm then they do further down on the two sides. A similar result has been mentioned in one previous work, with no further investigation.[78] It is interesting to note that the 30-μm length is approximately equal to the length of a capillary loop in the dermal papillae in the skin outside of the cuticle area.[79] Capillary loops in dermal papillae are extensions of the sub-papillary plexus in the reticular dermis, and they are responsible for oxygen and nutrient transport to living cells in the epidermis. Because nails are specialized structures of the skin,[80] cuticle capillaries and dermal capillaries should be functionally similar parts of the capillary loop system (except that cuticle capillaries extend toward the distal nail bed), it will not be surprising to discover that the tip region of a cuticle capillary releases more oxygen than the other regions.

In Fig. 2.4(b) and (c), the RBC flow speed is reduced in the tip region (around 2/3 of the speed in the side regions). In blood rheology, RBC flow in capillaries is treated as a non-Newtonian fluid because of the special viscoelasticity of erythrocytes, which complicates the RBC flow in a capillary.[81–83] The reduced RBC flow speed may result from deformation of RBCs and a consequent change of their viscoelasticity while passing through the highly curved pathway of the tip region. Another possibility is that RBCs partially accumulate in the tip region. In order to test this hypothesis, we examined the hemoglobin concentration and the hemoglobin flux along the cuticles. Further, we used a paired *t*-test to compare the effects of the straight part and the curved part of a cuticle on the hemoglobin flow and concentration. To improve the statistical accuracy, we excluded outlier data points that have large standard deviations (>30%). It can be seen that this hypothesis is not supported by the results in Fig. 2.5(a) – (d), which show that both the flux of hemoglobin and the time-averaged hemoglobin concentration do not significantly differ between the side regions and the tip. Therefore, RBC flow is shown to be conserved along a cuticle capillary loop. The slower RBC flow in the tip region seems to meet a functional demand which requires a longer transit time of RBCs to release enough oxygen for metabolism. To investigate the relation between $D\mathrm{sO}_2$ and RBC flow speed, we calculated the time-derivative of sO_2 along cuticle capillary loops. Without introducing physical cuffing and compression on the arm imaged, and without any extra physiological stimulation, we assumed that the RBC flow can be considered as in a steady or quasi-steady state, which means $\frac{d(\mathrm{sO}_2)}{dt} = D\mathrm{sO}_2 \cdot \frac{ds}{dt} + \frac{\partial(\mathrm{sO}_2)}{\partial t} \approx D\mathrm{sO}_2 \cdot \frac{ds}{dt}$.[84] Fig. 2.5(e) and (f) show that RBCs release more oxygen per unit time in the tip region than in the sides. Although the statistics are not strongly significant ($p > 0.01$), this finding still suggests that there are factors other than RBC flow speed, such as partial oxygen pressure, that can drive RBCs to release more oxygen in the tip region.

In this investigation, our single-cell resolution OR-PAM system performed monitoring of several hemodynamic parameters on nine human volunteers. Cell-by-cell based statistics also provided insights. In the future, OR-PAM promises to help greatly in the early-stage diagnosis of perivascular diseases and to illuminate more fundamental mechanisms in hemodynamics.

2.5 Conclusions

In this chapter, the cuticle microcirculations of healthy volunteers were monitored by real-time single-cell resolution OR-PAM. Hemodynamic parameters such as C_{Hb}, sO_2, DsO_2, $v_{Hb,}$ and relative blood flow rate were extracted from the images. A drop in DsO_2 and slower RBC flow were observed in the tip region than in the side regions of a cuticle capillary loop. The conserved blood flow rate in a cuticle capillary loop and the drop in the time-derivative of sO_2 in the tip region suggest that the heterogeneity of the RBC flow speed over a cuticle capillary loop is not the only factor that determines the heterogeneity of the oxygen release in the loop.

Chapter 3 *In vivo* optical-resolution photoacoustic microscopy of sickle cell disease in humans

Hemolytic anemia and vaso-occlusive complications, such as recurrent and unpredictable pain crises, are widely experienced by patients with sickle cell disease. For the purpose of clinical diagnosis and development of treatment, numerous imaging techniques have been implemented to measure changes in the rheological properties of red blood cells, including their cellular morphology and flow rate. However, in order to evaluate the extent of sickle cell anemia and deoxygenation-dependent polymerization of abnormal hemoglobin, a more comprehensive tool for hemodynamic imaging of red blood cells is required. In this study, for the first time, high-speed optical-resolution photoacoustic microscopy (OR-PAM) has been demonstrated for monitoring micro-circulation in patients with sickle cell disease, via the readily accessible cuticle capillaries. Because OR-PAM can measure the relative oxygen concentration within red blood cells, metabolic information can be readily extrapolated. The results from PAM experiments show that, compared to the healthy subjects, sickle cell patients with a higher percentage of abnormal hemoglobin (> 90%), a slower blood flow speed, and a lower relative total concentration of hemoglobin. In addition, these patients seem to have denser cuticle capillaries in the nail-fold tissue than healthy subjects, possibly to compensate for the lower oxygen release rate in a single capillary.

3.1 Background

Sickle cell disease (SCD) is named for the shape of erythrocytes with polymerized abnormal hemoglobin under deoxygenized conditions.[85] As an inherited blood disorder, the abnormal hemoglobin results from mutations on the *HBB* gene that cause a replacement of a glutamic acid with valine in beta-globin, a sub-unit of a hemoglobin protein.[86] Patients with SCD usually suffer from numerous complications as they live longer, such as hemolytic anemia, recurrent painful crises, bacterial infection, cardiopulmonary organ dysfunction, chronic kidney injury, acute chest syndrome, and stroke.[87–89] Although there are only around 100,000 domestic patients, the estimated annual medical costs for SCD patients in the United States are more than 1.1 billion dollars.[90]

In order to understand the pathogenesis due to veso-occlusion caused by deformed red blood cells (RBCs), investigations have been reported on rheological properties such as Young's modulus, membrane plasticity, morphological variation, and cytoplasmic viscosity, as well as the kinetics of oxygenation.[91–96] Clinical assessment of vascular abnormalities has also been widely conducted to develop new therapies and discover pre-mature complications. For instance, computer-assisted intra-vital microscopy, which is able to image blood flow with micrometer resolution, has been applied to observe bulbar conjunctival vessels and nail-fold capillaries in SCD patients.[97,98] In addition, macular vascular abnormalities in SCD patients have also been identified by ophthalmoscopy and spectral-domain optical coherent tomography (SD-OCT).[99,100] To assess the correlation between cerebral blood flow and stroke risk in SCD patients, transcranial Doppler ultrasonography (TCD) and conventional tomographic imaging techniques,

such as magnetic resonance imaging (MRI), positron emission tomography (PET), and single-photon emission computed tomography (SPECT), have proved to be adequate techniques.[101–112]

The stroke risk in SCD patients can be estimated by assessing cerebral blood hemodynamics using MRI-assisted TCD.[113] However, to figure out the etiology of other veso-occlusive-associated complications, such as episodic painful crises, and to provide fast and frequent screening for clinical diagnosis, there is still a need for a convenient and comprehensive technique that can monitor vascular hemodynamics.

Previously we have demonstrated that OR-PAM is capable of acquiring capillary vasculature and multiple hemodynamic parameters, such as the saturation of oxygen (sO_2), flow speed (v), relative hemoglobin concentration [HbT], and metabolic rate of oxygen (MRO_2), *in vivo* and non-invasively.[71,73–76,103,114] In this study, we monitored these hemodynamic parameters with OR-PAM in SCD patients in a steady disease state and compared the results with the same parameter values from healthy subjects. Our results show a lower flow speed and lower hemoglobin concentration in SCD patients, as well as different, but not always significantly different, values for the oxygen extraction fraction (OEF), blood flow rate (BF), and MRO_2. Our study not only benefits research on sickle cell disease but also verifies that OR-PAM can be a powerful tool for clinical diagnosis.

3.2 Methods

This study followed protocols approved by the Institutional Review Board of Washington University in St. Louis. Informed consent was obtained from all participants before any investigation was initiated.

3.2.1 Human subjects

We recruited six patients (19 to 42 years old, four men and two women) with HbSS (five subjects) or HbSC diseases (one subject) and seven healthy subjects (20 to 55 years old, two men and five women) from the clinics at the Washington University Medical Center. For each participant, a blood test was performed for Hb analysis, followed by OR-PAM imaging.

3.2.2 Imaging Procedures

We implemented dual-wavelength OR-PAM on capillaries in close proximity to the nail-fold cuticle region, which is easily accessible by the OR-PAM system and where the skin is thin enough to measure oxygen-metabolic parameters accurately. Participants first rested in a temperature-controlled laboratory (at 20 ^{o}C) for 15 minutes in order to reduce the effects of exertion. The left forearm of the participant was positioned horizontally on a custom-made hand platform with the palm down, and the fourth finger (the ringer finger) was fitted in a holding groove. Alcohol swabs were used to clean the image region, then a layer of ultrasound gel was applied, and finally the water holder for coupling PA signals to the imaging system was placed in contact atop the finger. During the entire experiment, we checked the status of the participants frequently to minimize the possibility of occluded blood flow resulting from an uncomfortable posture.

The imaging procedure consisted of both wide-field and high-speed dynamic imaging. Wide-field volumetric images (c-scan) had 2 × 2 × 0.5 mm dimensions on average and were used to assess the anatomic differences of capillaries in healthy subjects and patients. The acquisition time for each wide-field image was approximately 60 seconds. High-speed dynamic imaging recorded the oxygen-metabolic dynamics of red blood cells in a single capillary with a c-scan

rate between 12 – 20 Hz, depending on the dimensions of the capillary. The recording time for each capillary was 90 seconds. For each participant, we acquired two or three wide-field images and made seven to fifteen high-speed dynamic recordings. The total experimental time for each participant was less than one and a half hour, with short breaks upon request.

3.2.3 Optical-resolution photoacoustic microscopy

The dual-wavelength OR-PAM system is illustrated in Figure 3.1. Two nanosecond pulses (< 10 ns) at wavelengths of 532 nm (SPOT, Elforlight, Northants, UK) and 559 nm (INNOSLAB, Edgewave, Würselen, Germany) were guided to a home-built PA imaging probe.[85] The delay between the pulses was set at 10 μs to prevent overlapping of the generated PA signals. This system provided 3-μm lateral resolution and 15-μm axial resolution, based on the shift-and-sum of the un-enveloped PA signals.[86] The PA signals were then amplified (ZFL-500LN+, Mini-circuits, NY, USA), filtered, and fed into a 12-bit commercial waveform digitizer (ATS9350, Alazar Tech. Inc., QC, Canada). Raster scanning was provided by a voice coil motor (VCS-10, Equipment Solution, CA, USA) for the fast axis and a high-precision step motor (PLS–85, PI miCos, Eschbach, Germany) for the other axis. To measure the oxygen-metabolic parameters, a synchronized photodiode was used to monitor the energy from the lasers, pulse by pulse. The pulse energies used for exciting PA signals in each experiment were within the ANSI laser safety limit (20 $mJ \cdot cm^{-2}$). A field-programmable gate array card (FPGA) (PCI-7841, National Instruments, TX, USA) was programmed to synchronize all trigger signals.

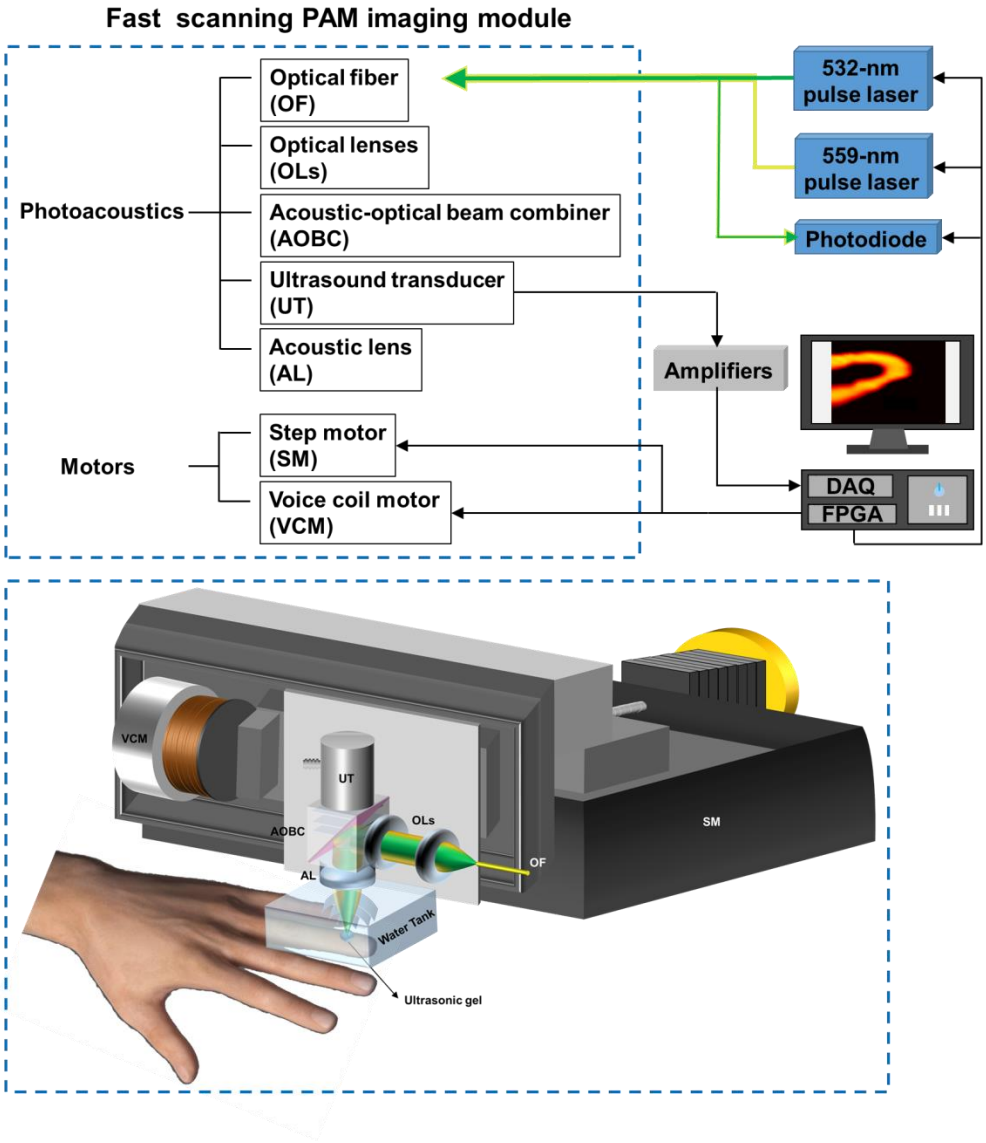

Figure 3.1 Schematic of the single-cell-resolution PAM system.

3.2.4 Imaging processing and analysis

To produce top-view images, maximum amplitude projection (MAP) along the depth direction was implemented on all acquired volumetric images. A contrast-to-noise ratio of 6 dB was set to segment capillaries from background. The mean capillary density was measured from segmented wide-field mages. Intensity-based automated registration was performed on frames of the MAP time-lapse videos acquired in high-speed dynamic mode. The registration threshold was set as

0.65 to screen out frames with too many artifacts to be processed. Implementing the methods proposed in previous reports,[85,87] we measured multiple oxygen-metabolic parameters, including the oxygen saturation (sO_2), oxygen extraction factor (OEF), speed of blood flow (v), blood flow rate, hematocrit (Hct), relative mean corpuscular hemoglobin concentration (MCHC), relative oxygen release rate (rO_2), and relative metabolic rate of oxygen (MRO_2):

$$\mathrm{OEF} = \frac{\mathrm{sO_{2\,in}} - \mathrm{sO_{2\,out}}}{\mathrm{sO_{2\,in}}}, \tag{3.1}$$

$$\mathrm{BF} = \frac{\pi}{4} * \mathrm{D}^2 * v, \tag{3.2}$$

$$\mathrm{rO_2} = \xi * (\mathrm{sO_{2\,in}} - \mathrm{sO_{2\,out}}) * \mathrm{C_{HbT}} * \mathrm{BF}, \tag{3.3}$$

$$\mathrm{MRO_2} = \frac{\mathrm{rO_2}}{\mathrm{W}} \sim \rho_{\#} * \mathrm{rO_2}, \tag{3.4}$$

where $\mathrm{sO_{2\,in}}$ and $\mathrm{sO_{2\,out}}$ denote the sO_2 on the upstream side and the downstream side of a capillary loop respectively, D is the mean vessel diameter, v is the flow speed, BF is the volumetric blood flow rate (in units of L/s), ξ is the oxygen binding capacity of hemoglobin (1.36 mL O_2/g), $\mathrm{C_{HbT}}$ is the average hemoglobin concentration, W is the average mass of the tissue fed by a capillary (in units of g), and $\rho_{\#}$ is the number density of the capillaries. We assumed the specific weight of nailfold tissue to be 1.0 g/cm^{3,} so W is proportional to the draining volume of a capillary.

3.2.5 Data analysis

To assure validity, an acquired time-lapse video was excluded if the frames screened out by the registration program exhibited too many temporal discontinuities to calculate the dynamic

changes of flow speed in at least three different moments. A participant's dataset was also excluded if the time-lapse video recorded fewer than five different capillaries.

3.3 Results

3.3.1 Oxygen consumption in cuticle capillaries

Table 1 lists the subjects included in this study (five patients, four healthy subjects) and the results of their blood tests. For sickle cell patients, bopth the total hemoglobin concentration and hemotocrit are obviously lower than for the control subjects, and PAM11 – 13 have more severe anemia than PAM01 and PAM07, since their Hct and [HbT] values are significantly lower. Figure 3.2(a) shows the time-averaged sO_2 along cuticle capillaries for the control group (with healthy subjects) of four healthy subjects and the patient group. The total sO_2 changes within the capillary loop are around 0.2 for both groups. Figure 3.2(b) shows the OEF for individual patients and the control group. Although the severity of sickle cell anemia varies among patients in this study, the time-averaged OEFs do not show significant differences compared to the control group.

ID	Age	Sex	Group	Hct (%)	[HbT] (%)	HbS (%)
PAM01	20	M	SCD	32.9	12	52.7
PAM07	19	M	SCD	31.9	11.9	79.9
PAM11	26	F	SCD	19.2	7.2	94.2
PAM12	20	M	SCD	25.5	8.8	94.0
PAM13	42	F	SCD	21.6	7.5	77.3
PAM04	19	F	Control	40.7	13.1	N/A
PAM06	55	F	Control	40.3	14.5	N/A
PAM08	27	F	Control	39.5	13.1	N/A
PAM10	21	F	Control	39.3	12.6	N/A

Table 3.1 Blood test results for selected subjects for data analysis. Hct, hemotocrit; [HbT], total hemoglobin concentration; HbS, abnormal hemoglobin. Patients are indicated by with light orange background, and the control group is indicated by a light blue background.

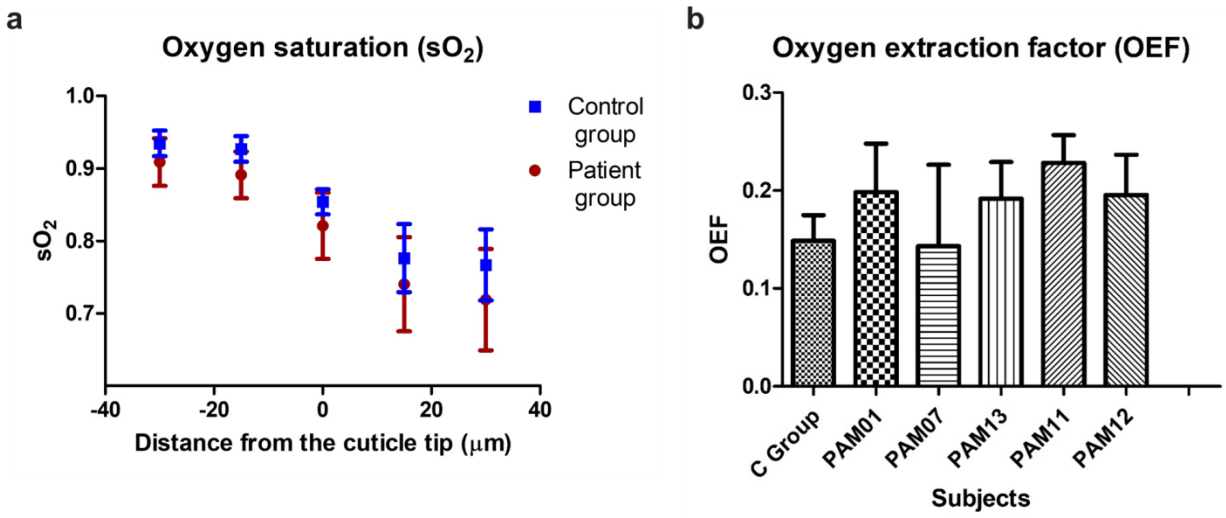

Figure 3.2 Time-averaged analysis of oxygen content. (a) Temporal average of sO_2 along the length of the cuticle capillaries for the control (healthy) group and the patient group. The position in a loop with the largest curvature is defined as 0 μm. (b) Oxygen extraction factors for the control group and individual patients, $n \geq 3$ for each subject. Error bar shows the standard error of measurement.

3.3.2 RBC flow in cuticle capillaries

High-speed scanning enables us to calculate flow speed from time-lapse images by Fourier analysis.[71,114] For a single capillary loop, a drop in flow speed through the tip of a capillary loop can be observed as we reported previously.[114] Figure 3.3(a) shows the statistics of time-averaged measurements of flow speed on two sides of capillary loops. Among the patient group, PAM11 and PAM12 have significant differences from the flow speed of the control group (*$P < 0.05$). To calculate blood flow (BF), we assumed the shape of the sides of a capillary loop can be approximated as a circular tube, and thus BF $\approx \pi * (\mathrm{d}_{\mathrm{side}}/2)^2 * v_{\mathrm{side}}$, where $\mathrm{d}_{\mathrm{side}}$ is the cross-sectional diameter of the loop on the sides that can be measured from the recorded images, and v is the flow speed at the same positon. The BF rates are shown in Figure 3.3(b). Basically, no significant difference can be found between the control group and individual patients.

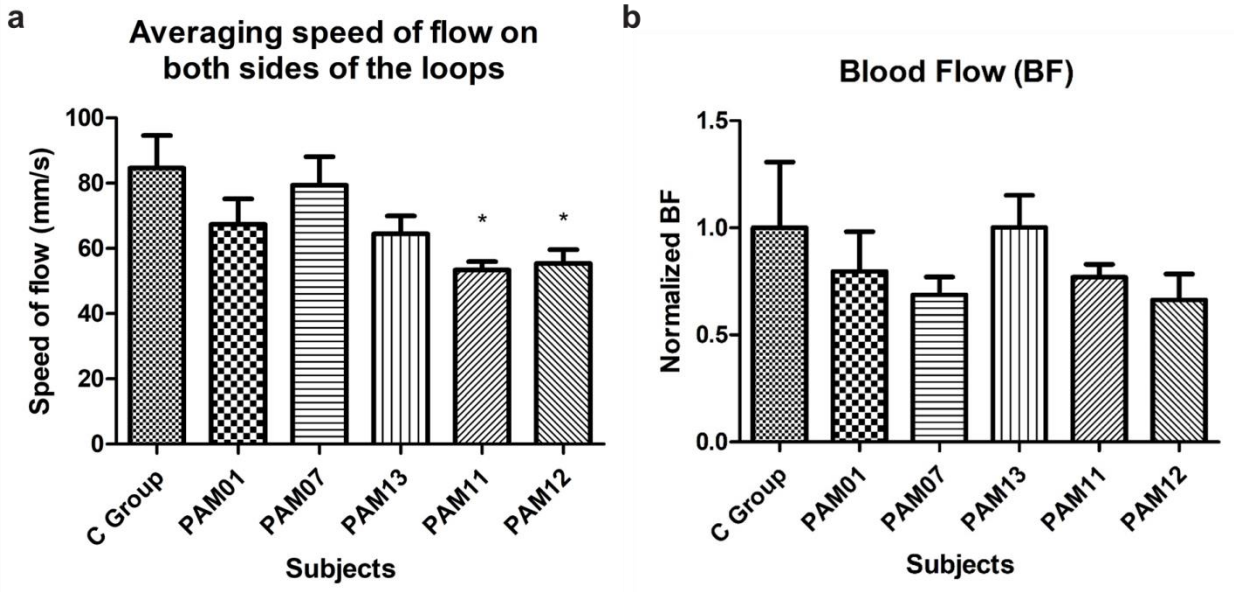

Figure 3.3 Time-averaged analysis of flow speed. Temporal average of (**a**) speed of flow and (**b**) blood flow rate for control group and individual patients. Statistics: unpaired Student's *t*-test *$P < 0.05$, $n \geq 3$ for each subject. Error bar shows the standard error of measurement.

3.3.3 Metabolic rate of oxygen

Figure 3.4 shows the measurement results for metabolic-related parameters. For PAM013, PAM11 and PAM12 patients, HbT is significantly different from the control group ($P < 0.01$). However, for rO_2, only PAM11 and PAM12 have statistical differences from the control group. In order to estimate the feeding volume of a single capillary for MRO_2 calculation, the average three-dimensional density of cuticle capillaries was calculated from a wide-field C-scan (volumetric) image, as illustrated in Figure 3.5. The fed weights of tissue for PAM11 – 13 seem to be less than for the control group, although the statistics did not show significant differences in the fed weight of tissue between the control group and patients (unpaired Student's *t*-test, $P_{avg} \sim 0.08$ for PAM11 - 13). Unlike rO_2 in Figure 3.4(b), no significant difference was found in the MRO_2 results in Figure 3.4(d).

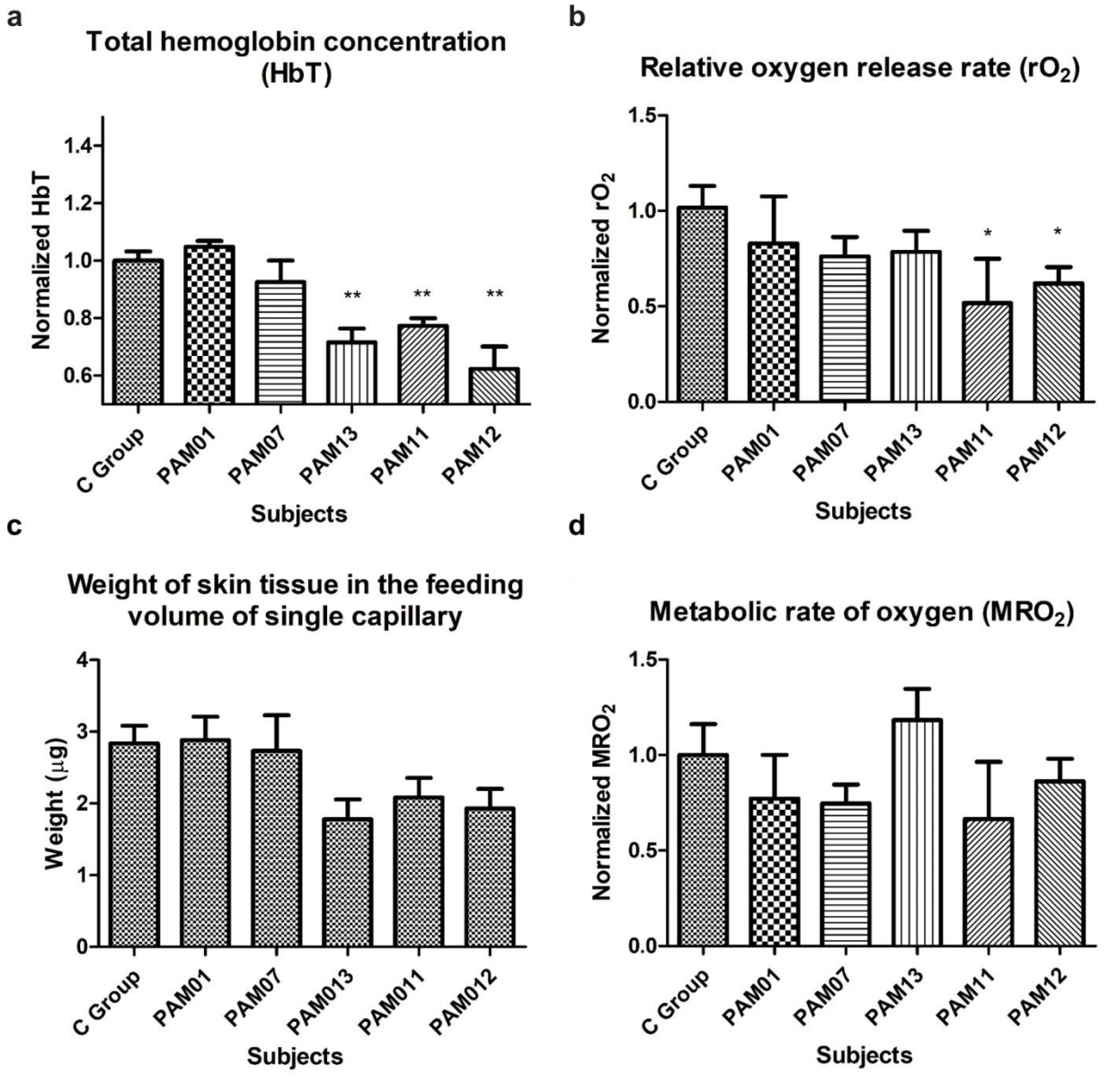

Figure 3.4 Time-averaged analysis of diverse parameters. Temporal average of (a) relative hemoglobin concentration, (b) oxygen release rate, (c) weight of tissue in the feeding volume of a single capillary, and (d) metabolic rate of oxygen for control group and individual patients. Statistics: unpaired Student's *t*-test $*P < 0.05$, $**P < 0.01$, $n \geq 3$ for each subject. Error bar: s.e.m.

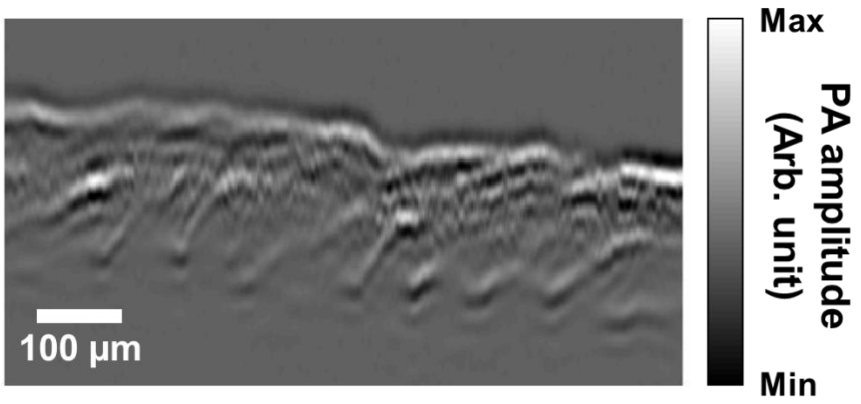

Figure 3.5 A B-scan image (cross-section view) shows oblique cuticle capillaries as well as melanin in both epidermis and dermis.

3.4 Discussion and Conclusion

In this study, we imaged capillary blood flow in both healthy subjects and SCD patients with high-speed and dual-wavelength OR-PAM and compared the differences in hemodynamics. The lateral resolution of the system we used was around 3 μm, which enabled us to localize single red blood cells flowing through a cuticle capillary loop when the RBCs were sparse enough (trickle flow).[114] Although the detailed morphology of sickle RBCs cannot be resolved with our system, it still could be useful to distinguish cells with large deformations. Interestingly, the proportion of images we acquired from SCD patients that capture single RBCs (seriously sickled or less deformed) was much less than for healthy subjects in the control group. This finding may result from the stronger adherence and lesser deformability of abnormal RBCs (even though hemoglobin molecules on the cell are not polymerized), so that abnormal RBCs more easily stick together in the blood flow. Moreover, sticky RBCs also more easily attach to vascular endothelium cells, which causes higher viscosity in the blood flow and hence a lower flow speed in capillaries,[86,89,91,97,98] which results in the slower flow speed we observed for the control

group, shown in Figure 3.3(a). Conversely, in large intracranial vessels such as the middle cerebral artery and internal carotid artery, published reports have noted that SCD patients have higher flow speed, which is also related to stenosis as well as to severe anemia and tissue hypoxia.[98,102,104,115] Our analysis of blood flow is shown in Figure 3.3(b), which is a product of flow speed and cross-sectional area of the capillary (data not shown). For the patient group, the averaged cross-sectional capillary area is slightly, but not significantly, larger than for the control group, which turns out to maintain the blood flow at levels without significant differences.

During the experimental period, none of the patients in this study was in a sickle cell crisis, so the patients were considered to be in steady state. The results shown in Figure 3.4(d) indicate that the oxygen demand of nailfold tissue for the patients was not significantly different from that of the control group. However, for PAM11 & PAM12, the rO_2 values are obviously lower than for the control group ($P < 0.05$), which means less oxygen was delivered by RBCs. We reason that this is the result of the lower total concentration of hemoglobin [Figure 3.4(a)], since no significant differences can be found in either OEF [Figure 3.2(b)] or BF [Figure 3.3(b)]. This situation may be clarified by Figure 3.4(c), which shows the fed skin tissue by a single capillary for the patient group is smaller than the control group.

The fed volume was estimated from the volumetric data we acquired during a wide-field C-scan image. It is defined as the product of two averaged lateral distances between two nearest capillary loops and the average depth of underlying vascular bed from which a capillary loop extends. For PAM11 – 13, the average capillary bed depths are 10 % - 20 % shallower than the control group, which may imply the cutaneous thicknesses are thinner for PAM11 – 13. We also note that PAM 11 - 13 have lower [HbT] and Hct, and higher HbS in their blood, so they are considered as more patients with more severe sickle cell anemia. Previous studies have reported

retinal thinning in SCD patients using OCT.[100,116] Arteriolar-occlusion-induced retinal ischemia was speculated to be the reason of the loss of inner retinal layers. However, cutaneous thinning has not been reported yet.

Our work in this study demonstrated that OR-PAM can measure multiple meaningful hemodynamic parameters that provide comprehensive information for clinical diagnosis. Further studies on the impact of SCD on the microvasculature will be helpful for developing better treatments and predicting the status of SCD patients more precisely.

Chapter 4 Dual-axis illumination for virtually augmenting the detection view of optical-resolution photoacoustic microscopy

Optical-resolution photoacoustic microscopy (OR-PAM) has demonstrated fast, label-free volumetric imaging of optical-absorption contrast within the quasi-ballistic regime of photon scattering. However, the limited numerical aperture of the ultrasonic transducer restricts the detectability of the photoacoustic waves, thus resulting in incompletely reconstructed features. To tackle the limited-view problem, we added an oblique illumination beam to the original co-axial optical-acoustic scheme to provide a complementary detection view. The virtual augmentation of the detection view was validated through numerical simulations and tissue-phantom experiments. More importantly, the combination of top and oblique illumination successfully imaged a mouse brain *in vivo* down to 1 mm in depth, showing detailed brain vasculature. Of special note, it clearly revealed the diving vessels, which were long missing in images from original OR-PAM.

4.1 Background

Photoacoustic (PA, also known as optoacoustic) tomography (PAT), based on the PA effect,[117,118] encompasses a collection of implementations, including PA microscopy (PAM) and PA computed tomography (PACT). Upon optical excitation by a short light pulse and the following energy conversion, the PA waves generated from excited molecules in the light-absorbing region always have positive initial pressures. Further, tissue boundaries, such as blood vessels, are usually acoustically smooth. Thus, the PA waves propagate normal to the local boundaries.[119] Consequently, the visibility of the boundaries in the reconstructed image depends on the detection angle and the position of the acoustic detector in the system.[120,121]

To completely reconstruct the features of an absorbing structure of arbitrary shape, ideally the PA signals should be acquired over all the solid angles spanned by the structure's boundary normal vectors, usually 4π steradians. However, a three-dimensional spherical transducer array is currently cost prohibitive, and scanning a detector to cover all solid angles is time-consuming. In fact, even in PACT, which desires full-view detection for reconstruction, hemispheric[122] and ring-shape[123] designs are more common in cutting-edge systems for practical applications, such as cerebral vascular imaging.[124] Even so, the cost for the entire detector array and corresponding data acquisition system remains a barrier to broader implementation.

On the other hand, scanning-based PAM can provide higher resolution within a shallower imaging depth in tissue, typically one order of magnitude less deep than PACT.[125] Accordingly, PAM, especially optical-resolution (OR) PAM, has been widely used to characterize features near the surface of tissue at various scales[56,126,127] or to image thin tissue slices.[111] Although the

illumination of PAM is localized compared to the wide-field illumination in PACT, PAM can still suffer from a limited detection view for specific absorber geometries.[128] However, implementing spherical detection would create further limitations on its applicability, and make it more difficult to maintain confocal alignment with the excitation beam for applications requiring fast scanning.[114,129]

Several alternative solutions have been proposed to overcome the limited view problem in PAT. Huang et al. used an acoustic reflector to create a mirror image of a transducer array orthogonal to the real one.[130] Shu et al. employed two linear transducer arrays[131] and Guo et al. rotated one linear array to increase the view angle.[121]

Apart from engineering improvements to acoustic detection, a solution from another perspective is to generate non-uniform excitation within a large homogeneous absorbing structure by engineering the optical illumination. Gateau et al.[132] demonstrated that the invisible structures in the original image could be retrieved by using dynamic speckles generated from a scattered coherent light source for non-uniform illumination. Wang et al.[133] used focused ultrasonic waves to thermally encode location information in the illuminated region.

However, none of these methods were tailored for or demonstrated on an OR-PAM system, although the concepts could be employed there as well. To date, there are only limited reports on the limited-view problem in PAM. For instance, Liu et al. exploited non-homogeneous illumination generated by an objective with a numerical aperture (NA) as high as 0.3 to increase the visibility of vertical structures imaged by OR-PAM.[128] Wang et al. generated non-uniform heating by a focused laser pulse preceding the excitation laser pulse, which enabled homogeneous structures to be imaged.[134]

In this study, we present an approach that is compatible with conventional OR-PAM and can virtually augment the detection view. This approach involves introducing a second illumination beam focused at the original confocal region, and around 45° off the axis of acoustic detection. As a result, structures along the direction of the acoustic axis that could not be imaged by the conventional top illumination beam can be imaged with the off-axis beam. For long structures along the oblique optical axis, the generated cylindrical PA waves are still detectable by the original ultrasonic transducer. Therefore, the oblique illumination provides a complementary detection view to the conventional OR-PAM. This approach allows the new system to inherit the original PA detection geometry, which provides excellent signal-to-noise-ratio (SNR). The first part of this paper describes numerical simulations to validate the efficacy of the proposed approach. Then the virtual augmentation of the detection view is demonstrated in a phantom experiment and by *in vivo* mouse brain imaging.

4.2 Numerical Simulation

To validate the virtually augmented detection view angle provided by dual-axis illumination PAM (DAI-PAM), we simulated the PA wave propagation from a vessel-mimicking phantom with two different orientations using the k-Wave toolbox.[135–137] Fig. 4.1(a) shows the schematic of the simulation and the phantom in the vertical orientation. The phantom was a two-dimensional absorptive bar that was 180-μm long and 15-μm wide. The sizes of the phantom were close to those of the cortical vessels of a mouse brain observed in a previous report.[138] The phantom was illuminated by a Gaussian beam focused by a lens (NA = 0.1) from the vertical and the oblique directions, respectively. We used a wavelength of 1045 nm to provide deeper imaging than possible with visible wavelengths.[61] Confocally aligned with the vertical beam, the

simulated ultrasonic transducer at the top had a 50 MHz central frequency, a 100% bandwidth, and an NA of 0.15. Images of the phantoms from both top illumination and oblique illumination were formed by raster-scanning over the horizontal and the vertical directions.

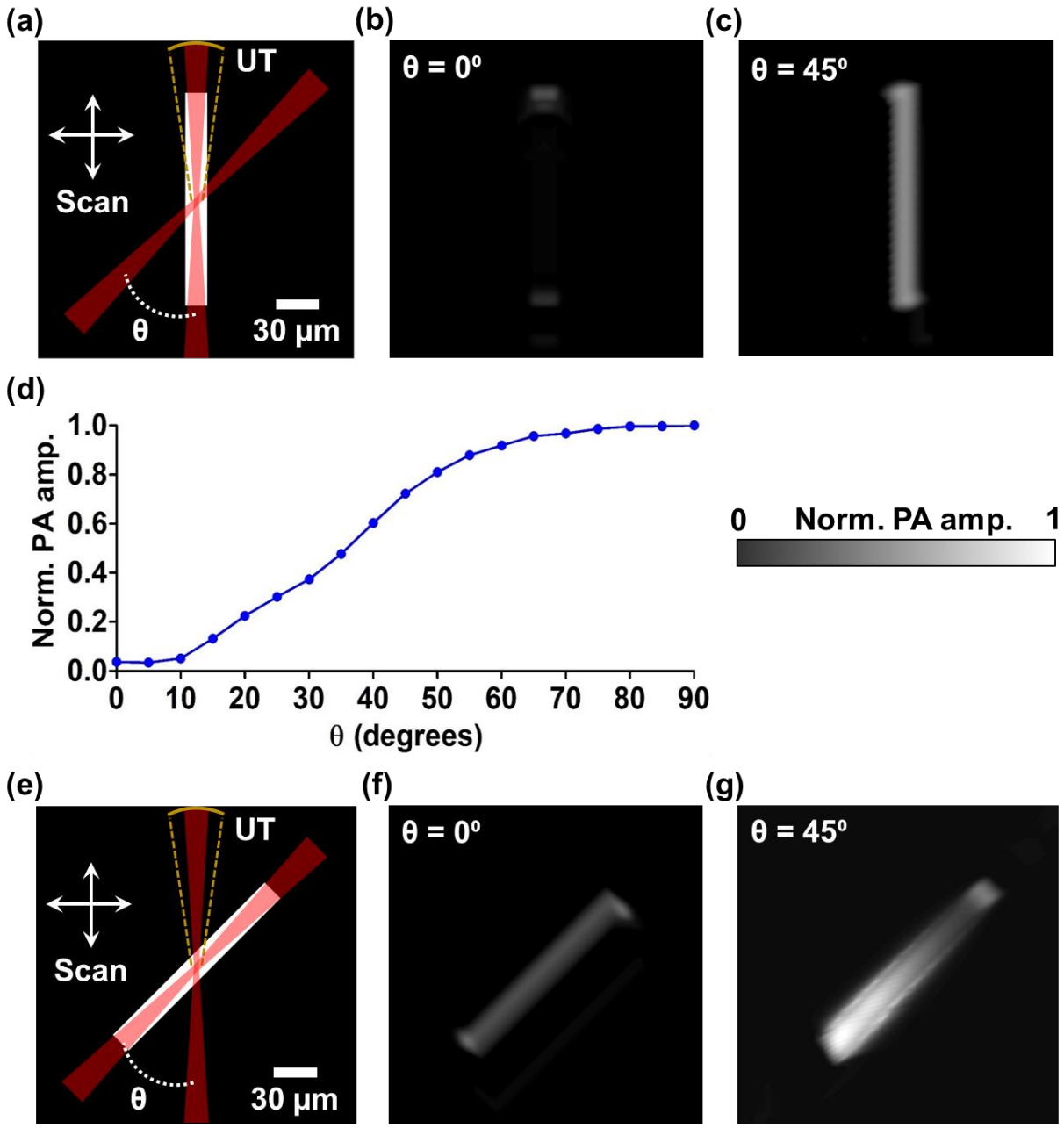

Figure 4.1 Numerical simulation of the virtually augmented view angle of DAI-PAM. (a) Schematics of the simulation for the vertical phantom, which was imaged respectively with two Gaussian beams, one

from the top, and the other from the upper right at an inclined angle θ (both with an NA = 0.1). The PA signals were detected by a focused ultrasonic transducer (UT) with an NA = 0.15 and a central frequency of 50 MHz. Two-dimensional scanning was applied to form an image. (b) – (c) The images formed by raster-scanning the phantom with the top and oblique illumination, respectively. The entire vertical feature was missed in (b). (d) The dependence of the received PA waves on the inclined angle. (e) Schematics of the simulation for the 45°-oblique phantom. (f) – (g) The images formed by raster-scanning the phantom with the top and oblique illumination at θ = 45°, respectively. The phantom absorber could be reconstructed with both the top and oblique illumination.

As seen in Fig. 4.1(b), the simulated image demonstrates the limited view for the vertical phantom in conventional OR-PAM. This phenomenon results from the long depth of focus of the top illumination beam (around 67 μm), where the illumination is relatively homogeneous and the energy deposition generates a cylindrical PA wave propagating horizontally. Therefore, the ultrasonic detector on top of the phantom vessel, with a fairly limited NA, can locate only the signals from the top and the bottom boundaries.

When the vertical phantom vessel is illuminated at 45°, the light-absorbing region reduces to an approximate acoustic point source and radiates spherical PA waves that are detectable by the top transducer. Presented in Fig. 4.1(c), the image formed by raster-scanning of the phantom shows improved visibility of the entire vertical vessel. Ideally, the efficiency of receiving cylindrical waves reaches the maximum when the beam has a 90° inclination. However, as shown in Fig. 4.1(d), even a 45° inclination provides a useful improvement (75% of the optimal performance) and is more compatible with most *in vivo* applications, where a reflection-mode geometry is preferred. These simulation results validate that these two illumination beams provide complementary detection views so that the entire detection view of the system is augmented.

A schematic of the simulation for the phantom in the oblique orientation of 45° to the vertical direction is presented in Fig. 4.1(e). Compared to the vertical phantom image, the structure of the oblique phantom can be fully reconstructed with the top illumination beam, as

shown in Fig. 4.1(f). The better visibility relative to the vertical phantom also results from the effect of acoustic point source radiation, which is similar to the case of the vertical phantom illuminated by the oblique beam.

Figure 4.1(g) presents a simulation where the oblique beam is used to illuminate the oblique phantom at the same inclined angle. In this case, the oblique illumination provides worse resolution for the oblique targets than the top illumination because of the larger illumination volume. The PA signals at different locations of the reconstructed image depend on the relative positions between the illuminated regions and the top transducer. Video 1 illustrates the propagation of the PA waves upon the optical excitation at three different locations on the phantom.

4.3 Methods

Figure 4.2 illustrates the experimental setup. A Q-switched Nd:YLF laser (<10 ns pulse duration, INNOSLAB, Edgewave) operated at wavelength of 1047 nm generates laser pulses for optical excitation. The laser beam is expanded and collimated by a convex lens and a concave lens to fill the back apertures of the vertical and oblique objectives. Then the laser beam passes through an optical spatial filter consisting of a pinhole and a 4F optical system to keep only the fundamental mode of the beam. A non-polarizing beamsplitter with 30:70 R:T ratio (BSS11, Thorlabs) splits the laser beam for direction to the vertical and the oblique objectives. Each lab-built objective lens assembly consists of an achromatic doublet (AC127-025-A, Thorlabs) and a correction lens to compensate for optical focusing in water. To set up the oblique illumination beam, a protractor was first used to coarsely align the lab-built objective lens with the vertical objective lens at an inclination of 45°. A digital camera was then employed to track the positions of the two focused

beam spots until fine confocal alignment was achieved. The acoustic detection was done by a custom-made focused ring-shaped ultrasonic transducer (35-MHz central frequency, 80% bandwidth, Resource Center for Medical Ultrasonic Transducer Technology, University of Southern California) with a 2-mm hole in the center for transmitting the laser beam. The focal zone of the ring transducer had a calculated lateral diameter of around 195 μm and was confocally aligned with the optical foci.

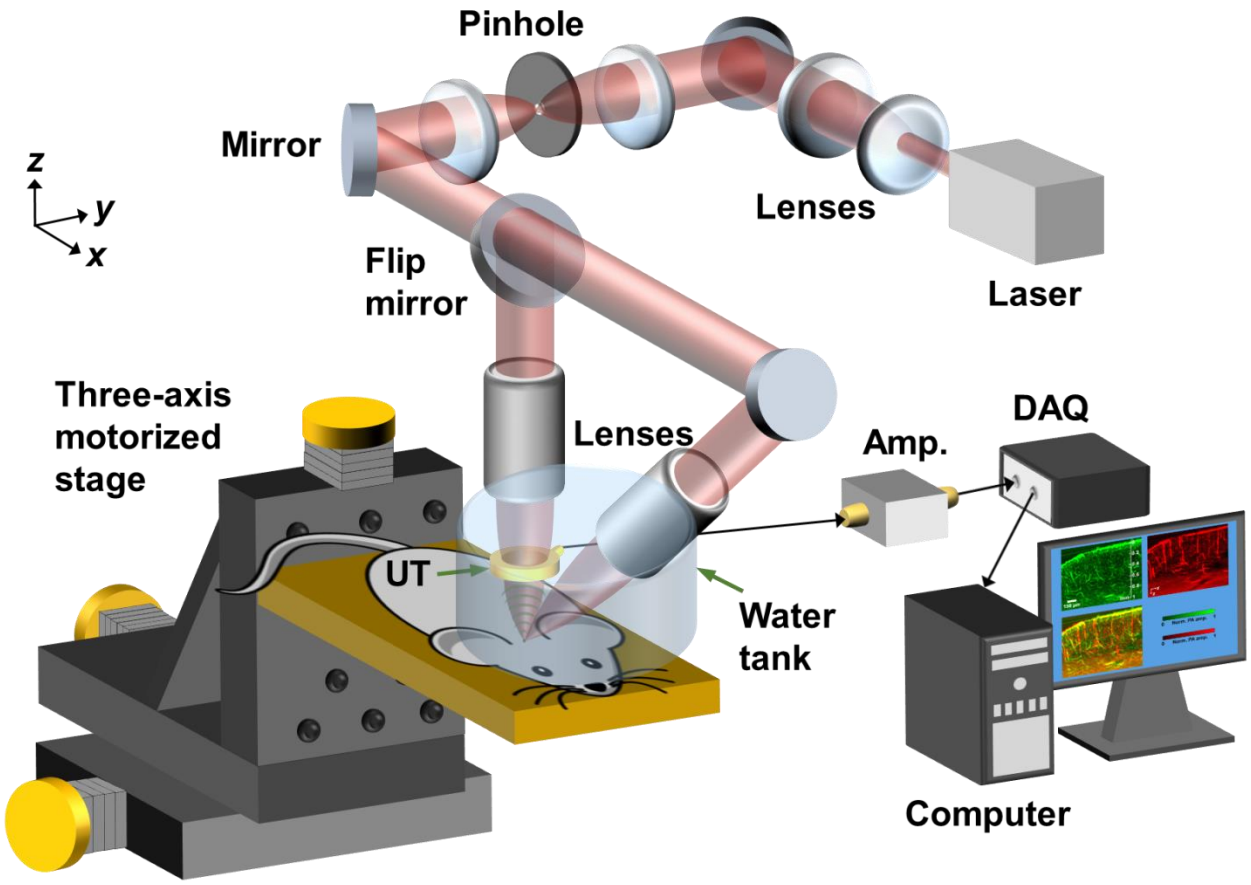

Figure 4.2 Schematic of DAI-PAM system. UT, ultrasonic transducer; Amp., amplifier; DAQ, data acquisition (DAQ) card. The beam was first expanded by a concave lens and a convex lens, then spatially filtered by a pinhole and a 4F optical system before focusing through the vertical and the oblique custom-designed objectives. Volumetric scans were done by three-axis motorized stages. The received PA signals were amplified and then acquired by a DAQ card before saving to a hard disk drive.

Images were formed by raster-scanning the object three-dimensionally with motorized translation stages (PLS-85, PI miCos GmbH), with a step size of 1.25 μm, which is around one third of the lateral resolution in each direction. For oblique illumination, each A-line in a B-scan image parallel to the *x*-*z* plane mapped to an obliquely illuminated region. Therefore, a proper shear transformation was implemented to recover the real geometry of the imaged objects.

To determine the inclined angle of the oblique illumination beam, we used the oblique illumination beam to acquire a B-scan image of a vertical hair phantom along the *x*-*z* plane (which contains the optical axes of both the top and oblique beams). The A-lines within the B-scan image contain PA signals generated from different regions on the phantom illuminated by different parts of the oblique beam. As a result, the B-scan image, shown in Fig. 4.3, profiles the spatial orientation of the oblique beam. The oblique angle can be determined to be 47.8° by fitting the pattern linearly with the least squares method.

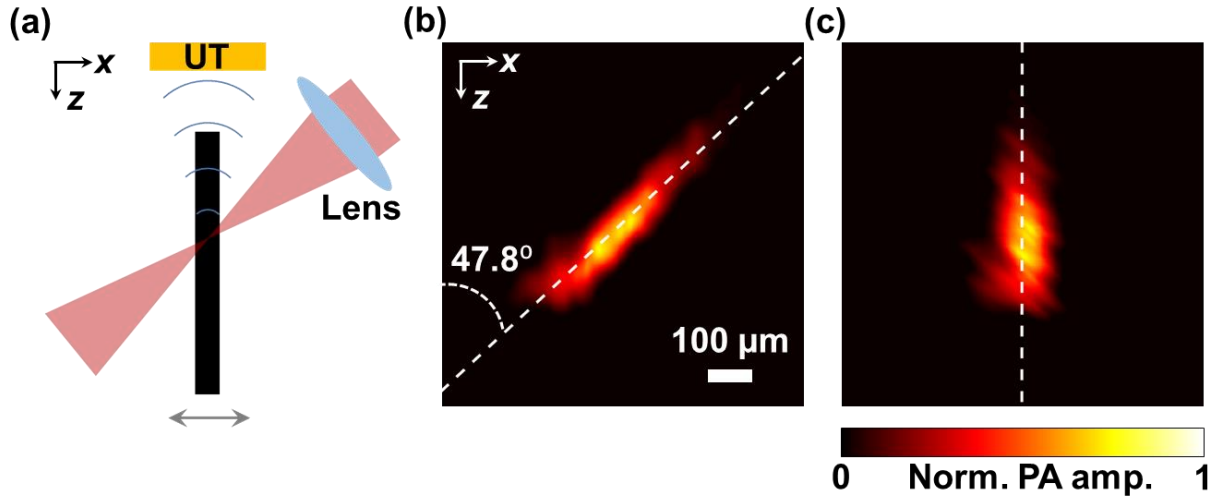

Figure 4.3 Phantom experiment for determining the inclined angle of the oblique illumination beam. (a) A vertically mounted hair phantom was imaged with the oblique illumination along the x-z plane to measure the inclined angle more precisely. (b) The original B-scan image profiled the orientation of the oblique beam. The inclined angle was calculated to be 47.8° after linear fitting by the least squares

method. (c) The real orientation of the object was recovered by implementing a proper shear transformation to the original B-scan image.

The lateral resolution for each beam was experimentally measured by imaging an Air Force resolution target (#58-198, Edmund Optics). A ring-shaped phantom (in the x-z plane) made of a knotted carbon fiber bundle embedded in 3% agar gel was then imaged to validate the virtual augmentation of detection view. In addition, a 6-week-old mouse brain was imaged in vivo as a demonstration. The mouse was anesthetized by isoflurane during the entire experiment. Craniotomy was performed on the parietal bone of the skull, and then images of the cerebral vasculature down to around 1 mm deep in the cortex were acquired. All experimental animal procedures were carried out in conformity with laboratory animal protocols approved by the Animal Studies Committee of California Institute of Technology.

4.4 Results

Figure 4.4(a) – (b) show images of the resolution target with the top and oblique illuminations, respectively. Based on the modulation transfer function analysis, the top illumination image has a cutoff spatial frequency at group 7, element 5 (G7E5) in both the *x* and *y* directions. However, the oblique illumination image shows an asymmetric lateral resolution, with a cutoff spatial frequency at group 7, element 1 (G7E1) in the *x* direction. The corresponding full width at half maximum (FWHM) resolutions are around 4.6 μm for G7E5 and 7.3 μm for G7E1, which are concordant with the edge profile analysis shown in Fig. 4.4(c) – (d).

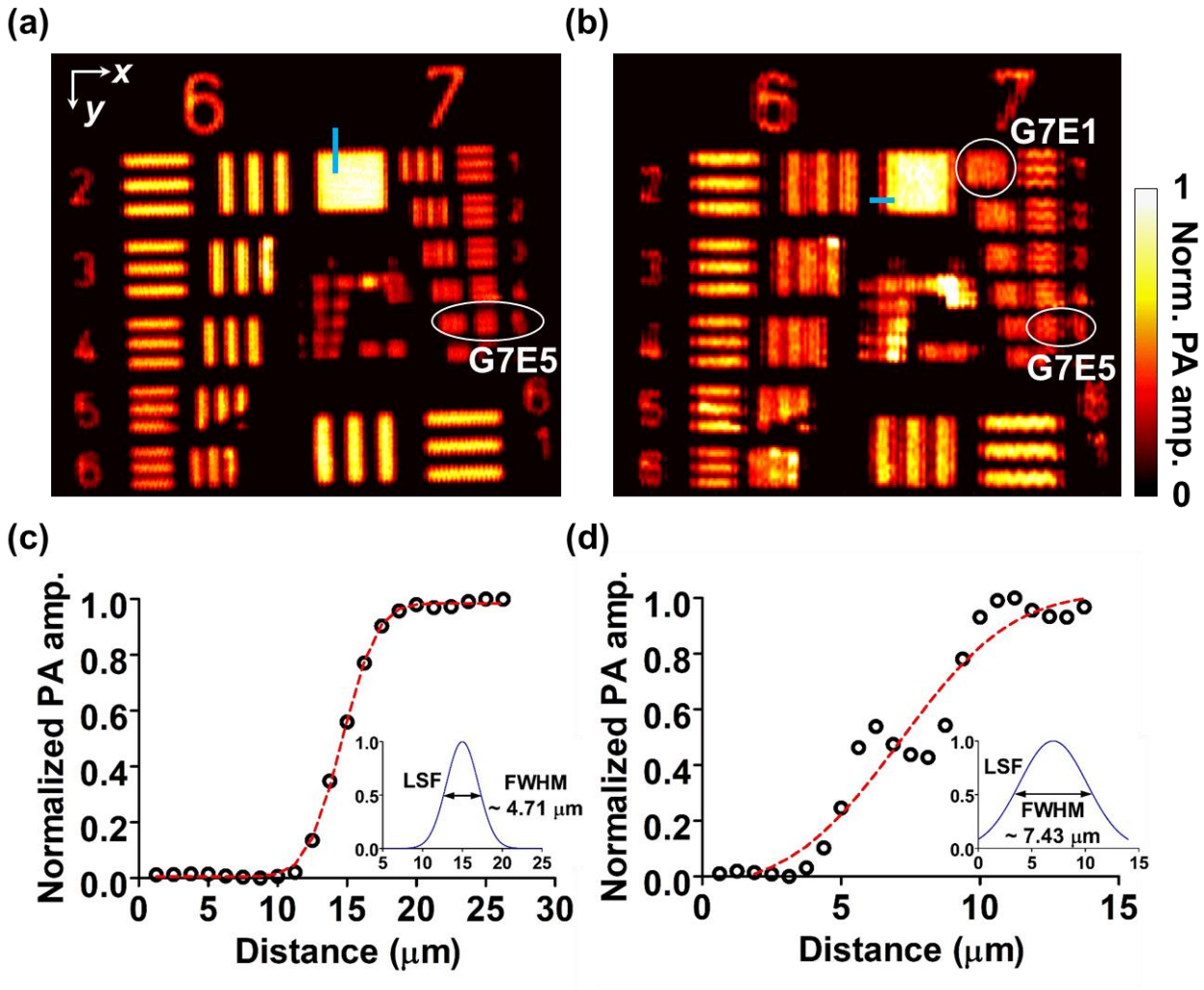

Figure 4.4 Spatial resolution tests of DAI-PAM with a USAF resolution target. (a) Imaging with the top illumination beam. Based on the modulation transfer analysis, the cut-off spatial frequencies in both the *x* and *y* directions were at group 7, element 5 (G7E5). (b) Imaging with the oblique illumination beam. The cut-off frequency in the *y* direction is the same as in (a), but the cut-off frequency in the *x* direction is at group 7, element 1 (G7E1). (c) – (d) Lateral resolution measured with the edge profile sampled from the thin blue areas in (a), and (b) respectively.

In addition to the degraded resolution in the *x* direction, the obliquely projected focal spot of the oblique illumination may also have introduced aberration into the image. For example, Fig. 4.4(b) shows some stripe artifacts around the group numbers. These may have resulted from the side lobes around the elliptical focal spot, and they deteriorate the image quality. Focus engineering can be implemented for side-lobe suppression and reduction of artifacts in the future.

Another phantom, shown in Fig. 4.5(a), consisting of five carbon fibers each with ~6-μm diameter was then imaged with both beams, as shown in Fig. 4.5(b) – (c). In the top illumination image, the PA amplitude significantly decreases as the boundary normal direction on the phantom approaches horizontal. In the oblique illumination image, the vertical parts on the two sides of the phantom remain discernible. By picking peak values from the amplitude profiles of the crossed lines at different angles (denoted by φ), the performance of the two illumination beams can be compared quantitatively, as presented in Fig. 4.5(d). For top illumination, the normalized average amplitude of the PA signals drops to around 0.12 when φ lies within the ranges of [–90°, –75°] and [75°, 90°]. For oblique illumination, in contrast, the average signals are around 0.5 within the same range, an improvement of roughly four times.

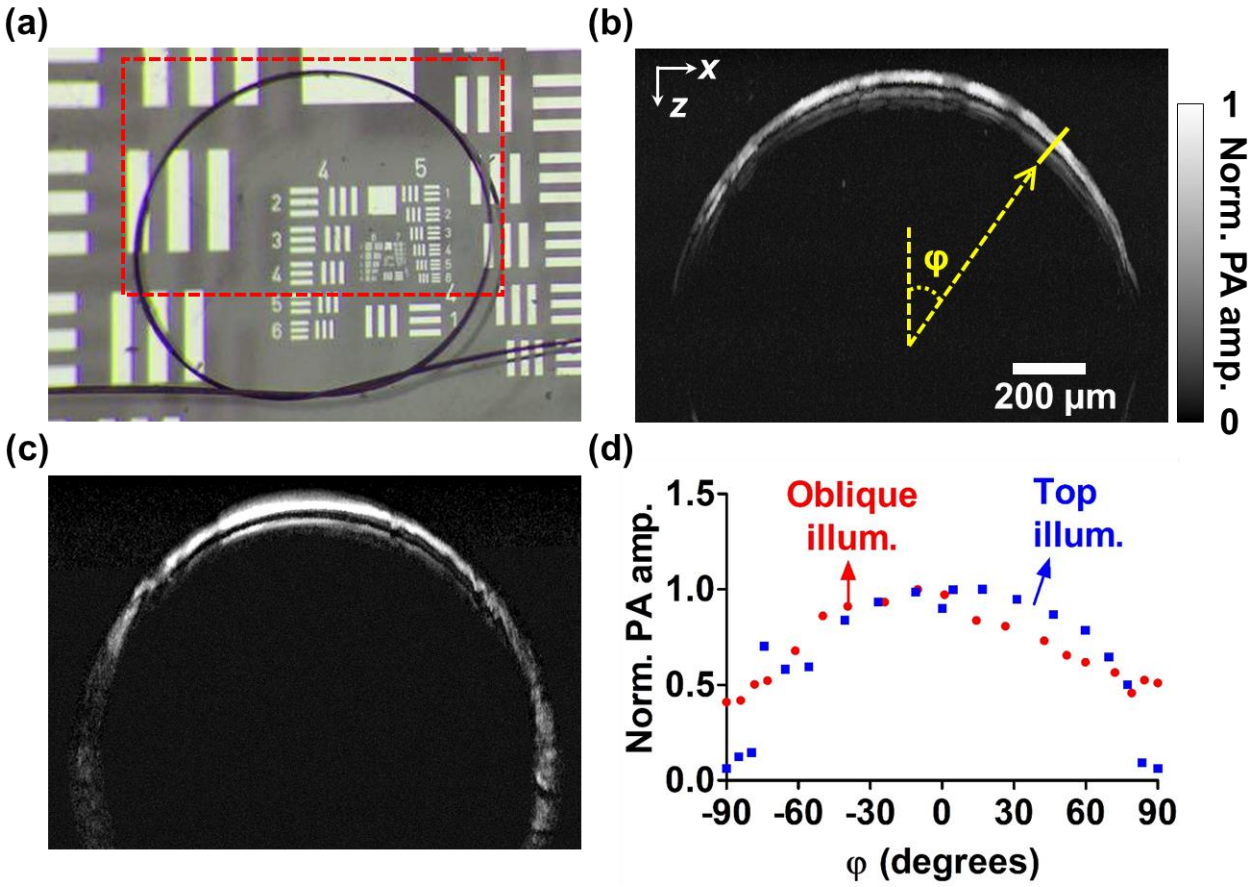

Figure 4.5 The circular phantom demonstrated the complementary view of the oblique illumination to the top illumination. (a) A photo of the phantom vessel comprised of five carbon fibers. Each of the fibers is around 6 μm in diameter. (b) – (c) Images of the phantom in the red dashed region with the top illumination beam and the oblique illumination beam, respectively. (d) Peak PA amplitudes sampled at different angles in (b) and (c), as illustrated by the yellow line in (b).

In Fig. 4.5(c), we noticed that the PA amplitude on the lower left side of the phantom image is less visible than on the lower right side. This phenomenon could still be observed when we imaged the phantom with a rotation of 180° along the *z*-axis, but with the signals recovered at a rotation angle of 90°. Therefore, we ruled out the possibility of artifacts in the phantom and thought the phenomenon could have resulted from shadowing[27] by the upper right side of the phantom (which partially blocked the oblique beam coming from the top right side), owing to the strong absorption of the thick fiber bundle.

A further demonstration was performed by *in vivo* mouse brain imaging. Fig. 4.6 presents maximum-amplitude-projected (MAP) images along the *y* direction with around 350-μm thickness. The top illumination image, in Fig. 4.6(a), shows abundant vasculature in the mouse cortex. However, several diving vessels that extend inward to the deeper brain from the surface of the cortex are invisible at greater depth. In contrast, the oblique illumination image in Fig. 4.6(b) clearly resolves the diving vessels. The overlaid image in Fig. 4.6(c), displays a dual-view mouse brain vascular image made with OR-PAM. Video 2 shows a volumetric rendering of the overlapped image. Increasing pulse energy along the imaging depth was used for both the top and oblique illumination, as presented in Fig. 4.6(d).

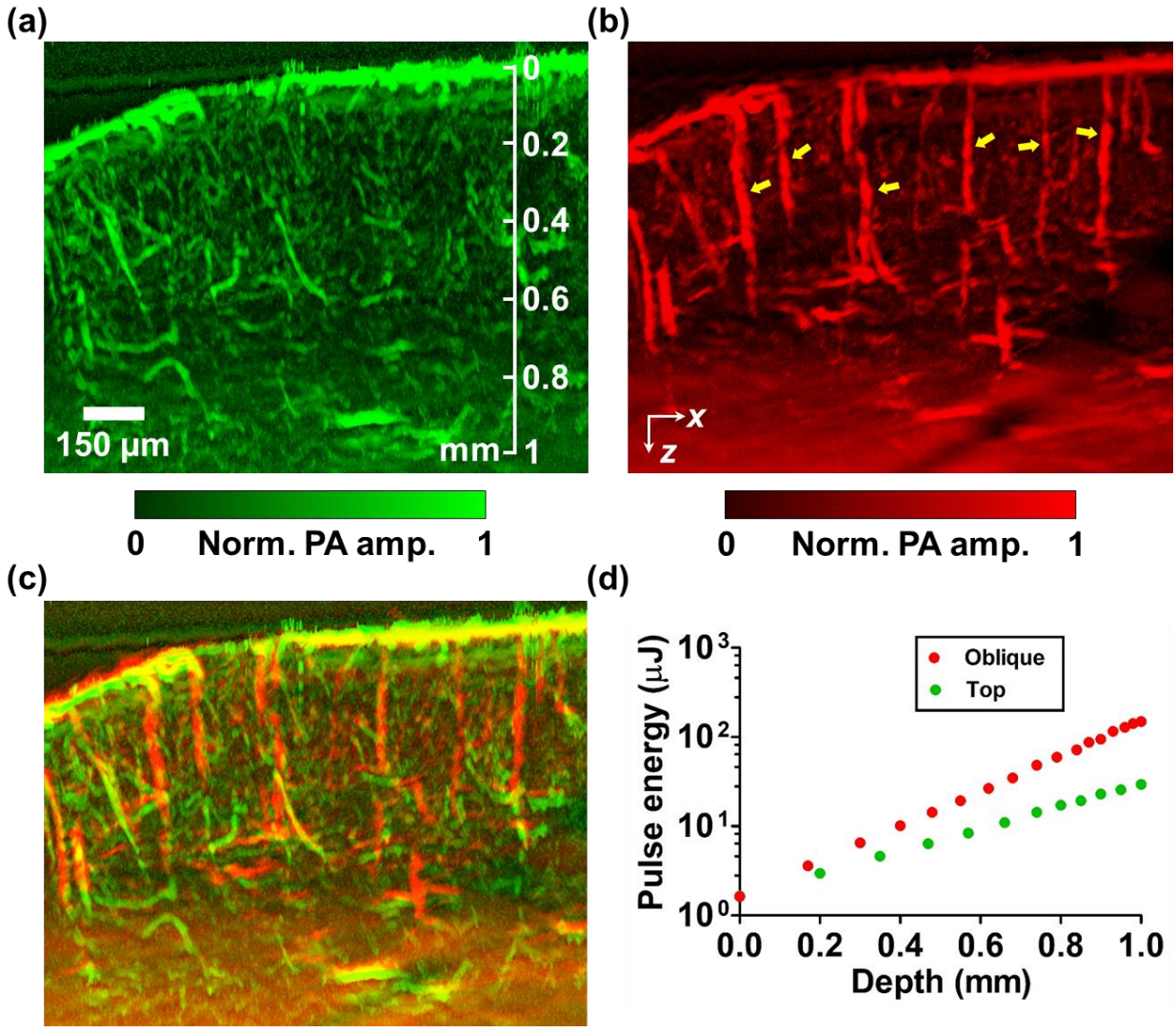

Figure 4.6 ***In vivo*** **DAI-PAM imaging of a mouse brain with** (a) the top illumination beam, and (b) the oblique illumination beam. The oblique illumination virtually augments the detection view so that vertical diving vessels (as illustrated by yellow arrows) become visible, unlike in the top illumination scheme of conventional OR-PAM. (c) Overlapped image presenting dual-view vasculature of the mouse cortex. (d) Pulse energies used at different depths for the top (green) and oblique (red) illuminations.

Figure 4.7(a) – (b) present top-view MAP images of a mouse cortex at various depths, imaged by the top and oblique beams, respectively. The MAP depth ranges are 35 μm for the top illumination images and 20 μm for the oblique illumination images, values that are within the focal depths along the *z* direction for these two illumination directions. To characterize the depth-dependent transition of lateral resolution, we analyzed the FWHM of the line profile (as

illustrated by the yellow bar in the images) across the tiniest vessel that could be found in the images at various depths, and quantified the corresponding contrast-to-noise ratios (CNRs) around the sampled regions, as presented in Fig. 4.7(c) – (d). With CNRs higher than 15 dB, the confidence of the measurements of the vessel diameters is higher than 99%. The imaged vessel diameters characterize the upper limits of the lateral resolution along the depth direction. The resolution significantly worsens at large depths. For the top illumination, the minimum vascular diameter imaged at 950 μm depth is twice the minimum diameter imaged on the surface. For the oblique illumination, doubling of the imaged minimum vascular diameter on the surface happens at 650 μm depth. This phenomenon reflects the different optical path lengths of the top beam and the oblique beam.

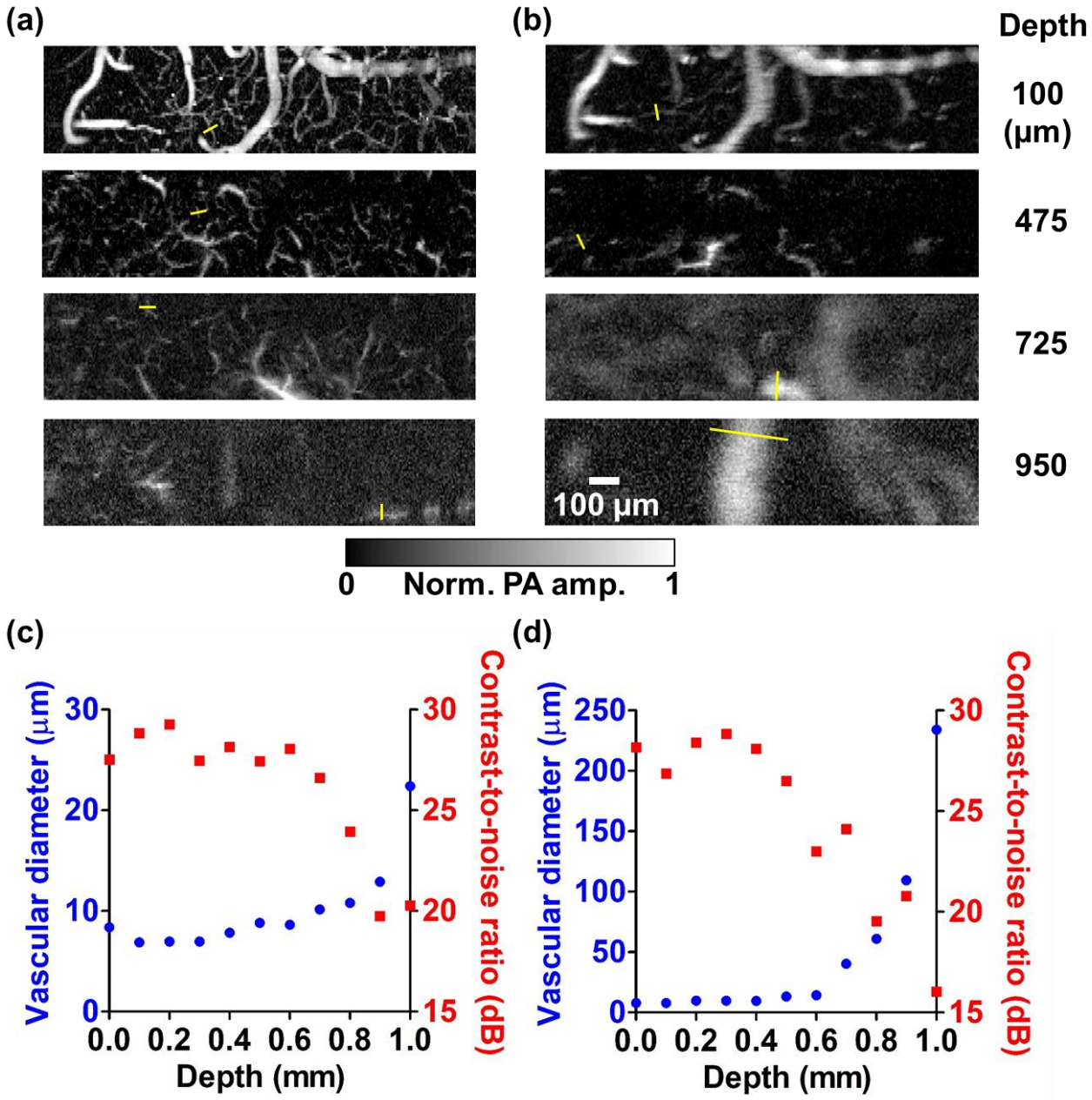

Figure 4.7 Maximum amplitude projection (MAP) images at different depths in a mouse brain acquired *in vivo*, and analysis of vascular diameters. The top illumination image in (a) displays more features than the oblique illumination image (b). The oblique illumination images start to blur at a shallower depth than the top illumination images because the lateral resolution is degraded by optical scattering due to the longer optical path length of the oblique illumination beam in the brain tissue. The depth-dependent lateral resolutions (shown in blue points) were characterized by picking out the smallest vessels within the field of view of the top illumination images (c) and the oblique illumination images (d), as illustrated by the yellow bars in (a) and (b). The corresponding estimated contrast-to-noise ratios (CNRs) around the sampled regions are shown in red squares in (c) and (d).

4.5 Discussion

In our previous study,[73] we demonstrated that PA signals propagating through ~1 mm of brain tissue and ~6 mm of water have a frequency spectrum that can be most readily detected with a 50-MHz transducer. Therefore, ideally we should have used a 50-MHz transducer in our experiments. However, the performance of custom-made, non-commercial ring transducers varies among different examples. Because of an obvious superiority in sensitivity, we chose to use a particular 35-MHz transducer in this study instead of other 50 MHz ring transducers available in the laboratory.

In addition to providing a complementary detection view to conventional OR-PAM, the off-axis geometry of the oblique illumination also offers advantages as dark field imaging, in which signals generated outside the overlapped region of the optical and the acoustic focal zones become less effective to be detected.[139] Therefore, surface signal shadowing, which is due to strong acoustic reverberation from absorbers at superficial depth such as highly dense vasculature in a mouse brain, can be reduced and the PA signals can be better revealed when imaging deep tissues.[140]

The spatial resolution of the oblique illumination in a plane normal to the inclined optical axis is optically determined and is the same as that of the top illumination. The resolution on the inclined optical axis is acoustically determined, and worse than the axial resolution of the top illumination by a factor of $\sec\theta$, owing to the inclination angle. However, in the laboratory coordinate system, the resolvability in the horizontal and vertical directions with the oblique illumination could be either optically or acoustically determined, depending on the structures to

be resolved. For a thin structure such as the coating on the resolution target, the resolvability in the horizontal or vertical direction was optically determined, as shown Fig. 4.4.

While performing the *in vivo* mouse brain imaging, optical attenuation, including absorption and scattering in the cerebral tissue, has to be taken into account. In our experiment, a near-infrared wavelength was used to increase the penetration depth over that available by visible wavelengths, where hemoglobin, has higher optical absorption.[61,141] In order to maintain a similar signal-to-noise ratio (CNR) at different imaging depths, the pulse energy was adaptively increased at greater depths. In addition, the increment of pulse energy along the depth was larger for the oblique illumination beam than for the top illumination beam, owing to the longer optical path length of that beam. At a depth of 1 mm, the ratio of pulse energies between the oblique and the top beams was around 5 for the two beams. The longer optical path length for the oblique illumination beam also results in faster deterioration of the optical focusing due to optical scattering. As seen in Fig. 4.7(b), below a depth of 0.8 mm, the lateral resolution was not enough to resolve small vessels that are visible in Fig. 4.7(a).

Currently, DAI-PAM imaging is demonstrated by raster-scanning the three-dimensional motorized stage holding the imaged object. For further applications such as full-view monitoring of cerebral hemodynamics, a higher imaging speed will be required. This can be implemented using the geometry of dual-beam illumination on a fast-scanning imaging head or by applying a tunable acoustic gradient lens.[142] Moreover, the degradation of lateral resolution due to optical scattering may be partially mitigated within a certain depth range by implementing PAM with adaptive optics.[143]

DAI-PAM could also benefit quantitative multi-wavelength PAM for measuring blood oxygenation in the cortex, such as the oxygen saturation in cerebral diving vessels demonstrated in this study. Because of the non-negligible wavelength-dependent light attenuation in deep tissue, the main challenge is getting accurate values of oxygen saturation in the quasi-diffusive regime (which, in a mouse brain, begins approximately at 950 μm for the top illumination and 650 μm for the oblique illumination, based on Fig. 4.7). By implementing either appropriate fluence models[144] or introducing another controlled mechanism that is invariant with the local fluence[145], it is feasible to solve the inverse problem and measure the concentrations of oxy- and deoxy-hemoglobin in the future.

4.6 Conclusion

In this study, we reported that adding an oblique illumination beam could effectively expand the detection view of conventional OR-PAM. We explained the mechanism through numerical experiments and demonstrated its feasibility by performing phantom experiments and *in vivo* mouse brain imaging. The dual-view results presented here show that DAI-PAM is promising for cerebral vascular imaging and is potentially useful for other biomedical applications, such as studying the angiogenesis of tumors or lymphatic imaging.

Chapter 5 Summary and Outlook

In this dissertation, PAM systems have been applied or developed for clinical investigation and fundamental science research, and demonstrated in studies of red-blood-cell dynamics in nailfold capillaries in healthy subjects and patients with sickle cell disease. We also present a dual-axis illumination system with an expanded detection view for imaging complete vasculature in bulk tissue.

In Chapter 2, we used high-speed PAM to investigate the red-blood-cell dynamics in individual capillaries in healthy subjects. We showed that the nailfold capillaries are in shape of well-aligned half loops toward the distal nail bed. Within individual capillaries, red blood cells tended to unload more oxygen in the tip region than on the two sides. In addition, RBCs also slowed down while passing through the tip region.

In Chapter 3, we compared multiple parameters related to capillary morphology and RBC dynamics between healthy subjects and patients with SCD. The statistical results support that patients with SCD have more tortuous capillaries, a higher number density of capillaries, higher OEF, slower flow speed, reduced [HbT], and more elongated RBCs in their blood. A correlation analysis between these parameters was also presented.

In Chapter 4, we demonstrated both numerically and experimentally how a limited view problem arises when imaging vertically-oriented structures with top-illumination PAM, and we proposed an oblique illumination technique to alleviate this limitation and reveal missing structures in conventional PAM. We also demonstrated the impact of this technique by imaging the cerebral vasculature of a mouse brain *in vivo* down to 1 mm in depth.

Although voice-coil based OR-PAM has provided significant RBC dynamics information, especially in measuring oxygen release by a single cell, further investigation of the interactions between RBCs in flowing blood requires advances in imaging resolution and speed. Microelectromechanical scanners and high repetition rate light sources can achieve imaging speeds of up to five times faster than translational motor-based scanning. The imaging resolution can be improved with a tightly focused optical design, along with a high frequency ring transducer with a low NA. Another critical direction is to investigate RBC dynamics during painful crises. Here, PAM can provide parameter measurements that illuminate the dynamic mechanisms causing these symptoms, and that lead to better treatments in the future.

DAI-PAM demonstrated complete vasculature imaging in bulk tissue and reduced the possible misinterpretation of images, with some reduction in imaging speed and penetration depth. Further engineering work on system integration and miniaturization for high-speed scanning is necessary for future applications, such as investigating neurovascular responses to stimulations. To push the penetration depth down to the diffusive regime, wavefront engineering techniques might be implemented in order to maintain the optical focusing in deep tissue.

References

1. Zhou, Y., Yao, J. & Wang, L. V. Tutorial on photoacoustic tomography. *J Biomed Opt* **21,** 61007 (2016).

2. Wang, L. V. Multiscale photoacoustic microscopy and computed tomography. *Nature Photonics* **3,** 503–509 (2009).

3. Wang, L. V. Tutorial on photoacoustic microscopy and computed tomography. *IEEE Journal of Selected Topics in Quantum Electronics* **14,** 171–179 (2008).

4. Lutzweiler, C. & Razansky, D. Optoacoustic imaging and tomography: reconstruction approaches and outstanding challenges in image performance and quantification. *Sensors* **13,** 7345–7384 (2013).

5. Kruger, R. A. *et al.* Dedicated 3D photoacoustic breast imaging. *Medical Physics* **40,** 113301 (2013).

6. Deán-Ben, X. L. *et al.* Functional optoacoustic neuro-tomography for scalable whole-brain monitoring of calcium indicators. *Light: Science & Applications* **5,** e16201–e16201 (2016).

7. Wang, X. *et al.* Noninvasive laser-induced photoacoustic tomography for structural and functional *in vivo* imaging of the brain. *Nature Biotechnology* **21,** 803–806 (2003).

8. Xia, J. *et al.* Whole-body ring-shaped confocal photoacoustic computed tomography of small animals *in vivo*. *Journal of Biomedical Optics* **17,** 050506 (2012).

9. Piras, D., Wenfeng Xia, Steenbergen, W., van Leeuwen, T. G. & Manohar, S. G. Photoacoustic imaging of the breast using the twente photoacoustic mammoscope: present status and future perspectives. *IEEE Journal of Selected Topics in Quantum Electronics* **16,** 730–739 (2010).

10. Jathoul, A. P. *et al.* Deep *in vivo* photoacoustic imaging of mammalian tissues using a tyrosinase-based genetic reporter. *Nature Photonics* **9,** 239–246 (2015).

11. Yao, J., Ke, H., Tai, S., Zhou, Y. & Wang, L. V. Absolute photoacoustic thermometry in deep tissue. *Optics Letters* **38,** 5228 (2013).

12. Jo, J., Lee, C. H., Kopelman, R. & Wang, X. *In vivo* quantitative imaging of tumor pH by nanosonophore assisted multispectral photoacoustic imaging. *Nature Communications* **8,** (2017).

13. Benjamin, E. J., Blaha, M. J., Chiuve, S. E. & Mary, C. Heart disease and stroke statistics—2017 update: a report from the American Heart Association. 459

14. Taruttis, A. *et al.* Optoacoustic imaging of human vasculature: feasibility by using a handheld probe. *Radiology* **281,** 256–263 (2016).

15. Matsumoto, Y. *et al.* Label-free photoacoustic imaging of human palmar vessels: a structural morphological analysis. *Scientific Reports* **8,** (2018).

16. Toi, M. *et al.* Visualization of tumor-related blood vessels in human breast by photoacoustic imaging system with a hemispherical detector array. *Scientific Reports* **7,** (2017).

17. Zhou, Y. *et al.* Microcirculatory changes identified by photoacoustic microscopy in patients with complex regional pain syndrome type I after stellate ganglion blocks. *J Biomed Opt J Biomed Opt* **19,** (2014).

18. Yang, J.-M. *et al.* Simultaneous functional photoacoustic and ultrasonic endoscopy of internal organs *in vivo*. *Nature Medicine* **18,** 1297–1302 (2012).

19. Jeon, S. *et al. In Vivo* Photoacoustic imaging of anterior ocular vasculature: a random sample consensus approach. *Scientific Reports* **7,** (2017).

20. De Backer, D. *et al.* Monitoring the microcirculation in the critically ill patient: current methods and future approaches. *Intens Care Med Intens Care Med* **36,** 1813–1825 (2010).

21. De Backer, D., Donadello, K. & Cortes, D. O. Monitoring the microcirculation. *J Clin Monit Comput J Clin Monit Comput* **26,** 361–366 (2012).

22. LeRoy, E. C., Downey, J. A. & Cannon, P. J. Skin capillary blood flow in scleroderma. *Journal of Clinical Investigation* **50,** 930–939 (1971).

23. Murray, A. K. *et al.* Preliminary clinical evaluation of semi-automated nailfold capillaroscopy in the assessment of patients with Raynaud's phenomenonon. *Microcirculation Microcirculation* **18,** 440–447 (2011).

24. Rossi, D. *et al.* The role of nail-videocapillaroscopy in early diagnosis of scleroderma. *Autoimmun Rev Autoimmun Rev* **12,** 821–825 (2013).

25. Aellen, J. *et al.* Preserved capillary density of dorsal finger skin in treated hypertensive patients with or without type 2 diabetes. *Microcirculation Microcirculation* **19,** 554–562 (2012).

26. Levy, B. I. *et al.* Impaired tissue perfusion - A pathology common to hypertension, obesity, and diabetes mellitus. *Circulation Circulation* **118,** 968–976 (2008).

27. Vajkoczy, P., Ullrich, A. & Menger, M. D. Intravital fluorescence videomicroscopy to study tumor angiogenesis and microcirculation. *Neoplasia Neoplasia* **2,** 53–61 (2000).

28. Fantini, S. Dynamic model for the tissue concentration and oxygen saturation of hemoglobin in relation to blood volume, flow velocity, and oxygen consumption: Implications for functional neuroimaging and coherent hemodynamics spectroscopy (CHS). *Neuroimage Neuroimage* **85,** 202–221 (2014).

29. Yonekura, Y. *et al.* SPECT with [Tc-99m]-d,l-hexamethyl-propylene amine oxime (Hm-Pao) compared with regional cerebral blood-flow measured by PET - Effects of linearization. *J Cerebr Blood F Met J Cerebr Blood F Met* **8,** S82–S89 (1988).

30. Heeger, D. J. & Ress, D. What does fMRI tell us about neuronal activity? *Nat Rev Neurosci Nat Rev Neurosci* **3,** 142–151 (2002).

31. Tarkin, J. M., Joshi, F. R. & Rudd, J. H. F. PET imaging of inflammation in atherosclerosis. *Nat Rev Cardiol Nat Rev Cardiol* **11,** 443–457 (2014).

32. Dobrucki, L. W. & Sinusas, A. J. PET and SPECT in cardiovascular molecular imaging. *Nat Rev Cardiol Nat Rev Cardiol* **7,** 38–47 (2010).

33. Culver, J. P. *et al.* Diffuse optical tomography of cerebral blood flow, oxygenation, and metabolism in rat during focal ischemia. *J Cerebr Blood F Met J Cerebr Blood F Met* **23,** 911–924 (2003).

34. Schneider, A. G. *et al.* Renal perfusion evaluation with contrast-enhanced ultrasonography. *Nephrol Dial Transpl Nephrol Dial Transpl* **27,** 674–681 (2012).

35. Kalantarinia, K., Belcik, J. T., Patrie, J. T. & Wei, K. Real-time measurement of renal blood flow in healthy subjects using contrast-enhanced ultrasound. *Am J Physiol-Renal Am J Physiol-Renal* **297,** F1129–F1134 (2009).

36. Schneider, A. G. *et al.* Contrast-enhanced ultrasound evaluation of the renal microcirculation response to terlipressin in hepato-renal syndrome: a preliminary report. *Renal Failure Renal Failure* **37,** 175–179 (2015).

37. Awan, Z. A., Wester, T. & Kvernebo, K. Human microvascular imaging: a review of skin and tongue videomicroscopy techniques and analysing variables. *Clin Physiol Funct I Clin Physiol Funct I* **30,** 79–88 (2010).

38. Holowatz, L. A., Thompson-Torgerson, C. S. & Kenney, W. L. Last word on viewpoint: The human cutaneous circulation as a model of generalized microvascular function. *J Appl Physiol J Appl Physiol* **105,** 389–389 (2008).

39. Roustit, M. & Cracowski, J. L. Non-invasive assessment of skin microvascular function in humans: an insight into methods. *Microcirculation Microcirculation* **19,** 47–64 (2012).

40. Jung, F. *et al.* Primary and secondary microcirculatory disorders in essential-hypertension. *Clin Investigator Clin Investigator* **71,** 132–138 (1993).

41. Coulon, P., Constans, J. & Gosse, P. Impairment of skin blood flow during post-occlusive reactive hyperhemy assessed by laser Doppler flowmetry correlates with renal resistive index. *J Hum Hypertens J Hum Hypertens* **26,** 56–63 (2012).

42. Bukhari, M., Herrick, A. L., Moore, T., Manning, J. & Jayson, M. I. V. Increased nailfold capillary dimensions in primary Raynaud's phenomenon and systemic sclerosis. *Brit J Rheumatol Brit J Rheumatol* **35,** 1127–1131 (1996).

43. Herrick, A. L. The pathogenesis, diagnosis and treatment of Raynaud phenomenon. *Nat Rev Rheumatol Nat Rev Rheumatol* **8,** 469–479 (2012).

44. Kvandal, P., Stefanovska, A., Veber, M., Kvenumo, H. D. & Kirkeboen, K. A. Regulation of human cutaneous circulation evaluated by laser Doppler flowmetry, iontophoresis, and spectral analysis: importance of nitric oxide and prostaglandines. *Microvasc Res Microvasc Res* **65,** 160–171 (2003).

45. Attas, M. *et al.* Visualization of cutaneous hemoglobin oxygenation and skin hydration using near-infrared spectroscopic imaging. *Skin Res Technol Skin Res Technol* **7,** 238–245 (2001).

46. Murkin, J. M. & Arango, M. Near-infrared spectroscopy as an index of brain and tissue oxygenation. *British Journal of Anaesthesia* **103,** i3–i13 (2009).

47. Seo, I., Bargo, P. R. & Kollias, N. Simultaneous assessment of pulsating and total blood in inflammatory skin lesions using functional diffuse reflectance spectroscopy in the visible range. *J Biomed Opt J Biomed Opt* **15,** (2010).

48. Schwarz, B. *et al.* Effects of norepinephrine and phenylephrine on intestinal oyxgen supply and mucosal tissue oxygen tension. *Intens Care Med Intens Care Med* **27,** 593–601 (2001).

49. Hahn, M., Heubach, T., Steins, A. & Junger, M. Hemodynamics in nailfold capillaries of patients with systemic scleroderma: synchronous measurements of capillary blood pressure and red blood cell velocity. *J Invest Dermatol J Invest Dermatol* **110,** 982–985 (1998).

50. Wu, C. C., Zhang, G., Huang, T. C. & Lin, K. P. Red blood cell velocity measurements of complete capillary in finger nail-fold using optical flow estimation. *Microvasc Res Microvasc Res* **78,** 319–324 (2009).

51. Bauer, A., Kofler, S., Thiel, M., Eifert, S. & Christ, F. Monitoring of the sublingual microcirculation in cardiac surgery using orthogonal polarization spectral imaging. *Anesthesiology Anesthesiology* **107,** 939–945 (2007).

52. Genzel-Boroviczeny, O., Strotgen, J., Harris, A. G., Messmer, K. & Christ, F. Orthogonal polarization spectral Imaging (OPS): A novel method to measure the microcirculation in term and preterm infants transcutaneously. *Pediatr Res Pediatr Res* **51,** 386–391 (2002).

53. Treu, C. M., Lupi, O., Bottino, D. A. & Bouskela, E. Sidestream dark field imaging: the evolution of real-time visualization of cutaneous microcirculation and its potential application in dermatology. *Arch Dermatol Res Arch Dermatol Res* **303,** 69–78 (2011).

54. Choi, W. J., Wang, H. Q. & Wang, R. K. Optical coherence tomography microangiography for monitoring the response of vascular perfusion to external pressure on human skin tissue. *J Biomed Opt J Biomed Opt* **19,** (2014).

55. Baran, U., Shi, L. & Wang, R. K. K. Capillary blood flow imaging within human finger cuticle using optical microangiography. *J Biophotonics J Biophotonics* **8,** 46–51 (2015).

56. Hu, S., Maslov, K. & Wang, L. V. Second-generation optical-resolution photoacoustic microscopy with improved sensitivity and speed. *Opt Lett Opt Lett* **36,** 1134–1136 (2011).

57. Hu, S., Maslov, K., Tsytsarev, V. & Wang, L. V. Functional transcranial brain imaging by optical-resolution photoacoustic microscopy. *J Biomed Opt J Biomed Opt* **14,** (2009).

58. Yao, J. J., Maslov, K. I., Shi, Y. F., Taber, L. A. & Wang, L. H. V. *In vivo* photoacoustic imaging of transverse blood flow by using Doppler broadening of bandwidth. *Opt Lett Opt Lett* **35,** 1419–1421 (2010).

59. Ma, R., Söntges, S., Shoham, S., Ntziachristos, V. & Razansky, D. Fast scanning coaxial optoacoustic microscopy. *Biomed. Opt. Express, BOE* **3,** 1724–1731 (2012).

60. Deán-Ben, X. L. & Razansky, D. Functional optoacoustic human angiography with handheld video rate three dimensional scanner. *Photoacoustics* **1,** 68–73 (2013).

61. Hai, P., Yao, J., Maslov, K. I., Zhou, Y. & Wang, L. V. Near-infrared optical-resolution photoacoustic microscopy. *Optics Letters* **39,** 5192 (2014).

62. Hai, P. *et al.* Label-free high-throughput detection and quantification of circulating melanoma tumor cell clusters by linear-array-based photoacoustic tomography. *Journal of Biomedical Optics* **22,** 041004 (2016).

63. Hai, P., Yao, J., Li, G., Li, C. & Wang, L. V. Photoacoustic elastography. *Optics Letters* **41,** 725 (2016).

64. Hai, P., Zhou, Y., Gong, L. & Wang, L. V. Quantitative photoacoustic elastography in humans. *Journal of Biomedical Optics* **21,** 066011 (2016).

65. Hai, P., Zhou, Y., Liang, J., Li, C. & Wang, L. V. Photoacoustic tomography of vascular compliance in humans. *Journal of Biomedical Optics* **20,** 126008 (2015).

66. Ma, J., Shi, J., Hai, P., Zhou, Y. & Wang, L. V. Grueneisen relaxation photoacoustic microscopy *in vivo*. *Journal of Biomedical Optics* **21,** 066005 (2016).

67. Liang, J., Gao, L., Hai, P., Li, C. & Wang, L. V. Encrypted three-dimensional dynamic imaging using snapshot time-of-flight compressed ultrafast photography. *Scientific Reports* **5,** (2015).

68. Yang, J. *et al.* Motionless volumetric photoacoustic microscopy with spatially invariant resolution. *Nature Communications* **8,** (2017).

69. Wong, T. T. W. *et al.* Fast label-free multilayered histology-like imaging of human breast cancer by photoacoustic microscopy. *Science Advances* **3,** e1602168 (2017).

70. Zhou, Y. *et al.* Noninvasive determination of melanoma depth using a handheld photoacoustic probe. *Journal of Investigative Dermatology* **137,** 1370–1372 (2017).

71. Wang, L. D., Maslov, K., Yao, J. J., Rao, B. & Wang, L. H. V. Fast voice-coil scanning optical-resolution photoacoustic microscopy. *Opt Lett Opt Lett* **36,** 139–141 (2011).

72. Yeh, C., Soetikno, B., Hu, S., Maslov, K. I. & Wang, L. H. V. Three-dimensional arbitrary trajectory scanning photoacoustic microscopy. *J Biophotonics J Biophotonics* **8,** 303–308 (2015).

73. Yao, J. J. *et al.* High-speed label-free functional photoacoustic microscopy of mouse brain in action. *Nat Methods Nat Methods* **12,** 407-+ (2015).

74. Yao, J. J., Maslov, K. I., Zhang, Y., Xia, Y. N. & Wang, L. V. Label-free oxygen-metabolic photoacoustic microscopy *in vivo*. *J Biomed Opt J Biomed Opt* **16,** (2011).

75. Wang, L. D., Maslov, K. & Wang, L. H. V. Single-cell label-free photoacoustic flowoxigraphy *in vivo*. *P Natl Acad Sci USA P Natl Acad Sci USA* **110,** 5759–5764 (2013).

76. Zhang, H. F., Maslov, K., Sivaramakrishnan, M., Stoica, G. & Wang, L. V. Imaging of hemoglobin oxygen saturation variations in single vessels *in vivo* using photoacoustic microscopy. *Applied Physics Letters* **90,** 053901 (2007).

77. Wang, X., Xie, X., Ku, G., Wang, L. V. & Stoica, G. Noninvasive imaging of hemoglobin concentration and oxygenation in the rat brain using high-resolution photoacoustic tomography. *JBO, JBOPFO* **11,** 024015 (2006).

78. Hu, S. & Wang, L. H. V. Optical-resolution photoacoustic microscopy: auscultation of biological systems at the cellular level. *Biophys J Biophys J* **105,** 841–847 (2013).

79. Liao, Y. H. *et al.* Quantitative analysis of intrinsic skin aging in dermal papillae by *in vivo* harmonic generation microscopy. *Biomed Opt Express Biomed Opt Express* **5,** 3266–3279 (2014).

80. O'Rahilly, R. & Müller, F. *Basic Human Anatomy: A Regional Study of Human Structure*. (Saunders, 1983).

81. Dzwinel, W., Boryczko, K. & Yuen, D. A. A discrete-particle model of blood dynamics in capillary vessels. *J Colloid Interf Sci J Colloid Interf Sci* **258,** 163–173 (2003).

82. Sriram, K., Intaglietta, M. & Tartakovsky, D. M. Non-newtonian flow of blood in arterioles: consequences for wall shear stress measurements. *Microcirculation Microcirculation* **21,** 628–639 (2014).

83. Baieth, H. E. A. Physical parameters of blood as a non - newtonian Fluid. **4,** 7 (2008).

84. Zheng, Y. *et al.* A model of the hemodynamic response and oxygen delivery to brain. *Neuroimage Neuroimage* **16,** 617–637 (2002).

85. Dong, C., Chadwick, R. S. & Schechter, A. N. Influence of sickle hemoglobin polymerization and membrane properties on deformability of sickle erythrocytes in the microcirculation. *Biophysical Journal* **63,** 774–783 (1992).

86. Bunn, H. F. Pathogenesis and treatment of sickle cell disease. *New England Journal of Medicine* **337,** 762–769 (1997).

87. Gladwin, M. T., Sachdev, V., Jison, M. L. & Shizukuda, Y. Pulmonary hypertension as a risk factor for death in patients with sickle cell disease. *The New England Journal of Medicine* 10 (2004).

88. Gladwin, M. T. Cardiovascular complications and risk of death in sickle-cell disease. *The Lancet* **387,** 2565–2574 (2016).

89. Booth, C., Inusa, B. & Obaro, S. K. Infection in sickle cell disease: A review. *International Journal of Infectious Diseases* **14,** e2–e12 (2010).

90. McGann, P. T., Hernandez, A. G. & Ware, R. E. Sickle cell anemia in sub-Saharan Africa: advancing the clinical paradigm through partnerships and research. *Blood* **129,** 155–161 (2017).

91. Maciaszek, J. L. & Lykotrafitis, G. Sickle cell trait human erythrocytes are significantly stiffer than normal. *Journal of Biomechanics* **44,** 657–661 (2011).

92. Huang, Z. *et al.* Kinetics of increased deformability of deoxygenated sickle cells upon Oxygenation. *Biophysical Journal* **85,** 2374–2383 (2003).

93. Kviatkovsky, I. *et al.* Measuring sickle cell morphology during blood flow. *Biomedical Optics Express* **8,** 1996 (2017).

94. Byun, H. *et al.* Optical measurement of biomechanical properties of individual erythrocytes from a sickle cell patient. *Acta Biomaterialia* **8,** 4130–4138 (2012).

95. Kaul, D. K., Fabry, M. E., Windisch, P., Baez, S. & Nagel, R. L. Erythrocytes in sickle cell anemia are heterogeneous in their rheological and hemodynamic characteristics. *Journal of Clinical Investigation* **72,** 22–31 (1983).

96. Morris, C. L., Rucknagel, D. L. & Joiner, C. H. Deoxygenation-induced changes in sickle cell-sickle cell adhesion. *Blood* **81,** 3138–3145 (1993).

97. Lipowsky, H. H., Sheikh, N. U. & Katz, D. M. Intravital microscopy of capillary hemodynamics in sickle cell disease. *Journal of Clinical Investigation* **80,** 117–127 (1987).

98. Cheung, A. T. W. Microvascular abnormalities in sickle cell disease: a computer-assisted intravital microscopy study. *Blood* **99,** 3999–4005 (2002).

99. Roy, M. S., Gascon, P. & Giuliani, D. Macular blood flow velocity in sickle cell disease: relation to red cell density. *British Journal of Ophthalmology* **79,** 742–745 (1995).

100. Han, I. C., Tadarati, M. & Scott, A. W. Macular vascular abnormalities identified by optical coherence tomographic angiography in patients with sickle cell disease. *JAMA Ophthalmology* **133,** 1337 (2015).

101. Sarkar, S., Ghosh, S., Ghosh, S. K. & Collier, A. Role of transcranial Doppler ultrasonography in stroke. *Postgraduate Medical Journal* **83,** 683–689 (2007).

102. Cheung, A. T. W. Correlation of abnormal intracranial vessel velocity, measured by transcranial Doppler ultrasonography, with abnormal conjunctival vessel velocity, measured by computer-assisted intravital microscopy, in sickle cell disease. *Blood* **97,** 3401–3404 (2001).

103. Bernaudin, F. *et al.* Long-term treatment follow-up of children with sickle cell disease monitored with abnormal transcranial Doppler velocities. *Blood* **127,** 1814–1822 (2016).

104. Brass, L. M. *et al.* Middle cerebral artery blood velocity and cerebral blood flow in sickle cell disease. *Stroke* **22,** 27–30 (1991).

105. Behpour, A. M., Shah, P. S., Mikulis, D. J. & Kassner, A. cerebral blood flow abnormalities in children with sickle cell disease: a systematic review. *Pediatric Neurology* **48,** 188–199 (2013).

106. van den Tweel, X. W. *et al.* Cerebral blood flow measurement in children with sickle cell disease using continuous arterial spin labeling at 3.0-Tesla MRI. *Stroke* **40,** 795–800 (2009).

107. Al-Kandari, F. A. *et al.* Regional cerebral blood flow in patients with sickle cell disease: study with single photon emission computed tomography. *Annals of Nuclear Medicine* **21,** 439–445 (2007).

108. Kuo, W. C. *et al.* Virtual spatial overlap modulation microscopy for resolution improvement. *Optics Express* **21,** 30007 (2013).

109. Tseng, T. Y., Hsu, H. C., Yang, C. S., Tsai, T. H. & Dong, C. Y. Investigation of transport dynamics in oleic acid–induced transdermal drug delivery by two-photon fluorescence microscopy: an *ex-vivo* study of mouse skin. *Journal of Biomedical Optics* **18,** 096016 (2013).

110. Chen, Y. C., Hsu, H. C., Lee, C. M. & Sun, C. K. Third-harmonic generation susceptibility spectroscopy in free fatty acids. *Journal of Biomedical Optics* **20,** 095013 (2015).

111. Wong, T. T. W. *et al.* Label-free automated three-dimensional imaging of whole organs by microtomy-assisted photoacoustic microscopy. *Nature Communications* **8,** (2017).

112. Wong, T. T. W. *et al.* Whole-organ atlas imaged by label-free high-resolution photoacoustic microscopy assisted by a microtome. in (eds. Oraevsky, A. A. & Wang, L. V.) 93 (SPIE, 2018). doi:10.1117/12.2291056

113. Jordan, L. C., Casella, J. F. & DeBaun, M. R. Prospects for primary stroke prevention in children with sickle cell anaemia: Review. *British Journal of Haematology* **157,** 14–25 (2012).

114. Hsu, H. C., Wang, L. & Wang, L. V. *In vivo* photoacoustic microscopy of human cuticle microvasculature with single-cell resolution. *Journal of Biomedical Optics* **21,** 056004 (2016).

115. Bernaudin, F. *et al.* Long-term follow-up of pediatric sickle cell disease patients with abnormal high velocities on transcranial Doppler. *Pediatric Radiology* **35,** 242–248 (2005).

116. Witkin, A. J. Optical coherence tomography demonstration of macular infarction in sickle cell retinopathy. *Archives of Ophthalmology* **124,** 746 (2006).

117. Xia, J., Yao, J. & Wang, L. V. Photoacoustic tomography: principles and advances. 31 (2015).

118. Deán-Ben, X. L., Gottschalk, S., Mc Larney, B., Shoham, S. & Razansky, D. Advanced optoacoustic methods for multiscale imaging of *in vivo* dynamics. *Chemical Society Reviews* **46,** 2158–2198 (2017).

119. Guo, Z., Li, L. & Wang, L. V. On the speckle-free nature of photoacoustic tomography: On the speckle-free nature of photoacoustic tomography. *Medical Physics* **36,** 4084–4088 (2009).

120. Preisser, S. *et al.* Vessel orientation-dependent sensitivity of optoacoustic imaging using a linear array transducer. *Journal of Biomedical Optics* **18,** 026011 (2013).

121. Shu, W. *et al.* Broadening the detection view of 2D photoacoustic tomography using two linear array transducers. *Optics Express* **24,** 12755 (2016).

122. Kruger, R. A., Lam, R. B., Reinecke, D. R., Del Rio, S. P. & Doyle, R. P. Photoacoustic angiography of the breast. *Medical Physics* **37,** 6096–6100 (2010).

123. Xia, J., Chen, W., Maslov, K., Anastasio, M. A. & Wang, L. V. Retrospective respiration-gated whole-body photoacoustic computed tomography of mice. *Journal of Biomedical Optics* **19,** 016003 (2014).

124. Li, L. *et al.* Single-impulse panoramic photoacoustic computed tomography of small-animal whole-body dynamics at high spatiotemporal resolution. *Nature Biomedical Engineering* **1,** 0071 (2017).

125. Wang, L. V. & Yao, J. A practical guide to photoacoustic tomography in the life sciences. *Nature Methods* **13,** 627–638 (2016).

126. Estrada, H., Turner, J., Kneipp, M. & Razansky, D. Real-time optoacoustic brain microscopy with hybrid optical and acoustic resolution. *Laser Physics Letters* **11,** 045601 (2014).

127. Park, K. *et al.* Handheld photoacoustic microscopy probe. *Scientific Reports* **7,** (2017).

128. Liu, W. *et al.* Correcting the limited view in optical-resolution photoacoustic microscopy. *Journal of Biophotonics* **11,** e201700196 (2018).

129. He, Y. *et al. In vivo* label-free photoacoustic flow cytography and on-the-spot laser killing of single circulating melanoma cells. *Scientific Reports* **6,** (2016).

130. Huang, B., Xia, J., Maslov, K. & Wang, L. V. Improving limited-view photoacoustic tomography with an acoustic reflector. *Journal of Biomedical Optics* **18,** 110505 (2013).

131. Li, G., Li, L., Zhu, L., Xia, J. & Wang, L. V. Multiview Hilbert transformation for full-view photoacoustic computed tomography using a linear array. *Journal of Biomedical Optics* **20,** 066010 (2015).

132. Gateau, J., Chaigne, T., Katz, O., Gigan, S. & Bossy, E. Improving visibility in photoacoustic imaging using dynamic speckle illumination. *Optics Letters* **38,** 5188 (2013).

133. Wang, L., Li, G., Xia, J. & Wang, L. V. Ultrasonic-heating-encoded photoacoustic tomography with virtually augmented detection view. *Optica* **2,** 307 (2015).

134. Wang, L., Zhang, C. & Wang, L. V. Grueneisen relaxation photoacoustic microscopy. *Physical Review Letters* **113,** (2014).

135. Treeby, B. E. & Cox, B. T. k-Wave: MATLAB toolbox for the simulation and reconstruction of photoacoustic wave fields. *Journal of Biomedical Optics* **15,** 021314 (2010).

136. Cox, B. T. & Beard, P. C. Fast calculation of pulsed photoacoustic fields in fluids using *k* -space methods. *The Journal of the Acoustical Society of America* **117,** 3616–3627 (2005).

137. *MATLAB*. (The MathWorks, Inc.).

138. Horton, N. G. *et al. In vivo* three-photon microscopy of subcortical structures within an intact mouse brain. *Nature Photonics* **7,** 205–209 (2013).

139. Shelton, R. L. & Applegate, B. E. Off-axis photoacoustic microscopy. *IEEE Transactions on Biomedical Engineering* **57,** 1835–1838 (2010).

140. Maslov, K., Stoica, G. & Wang, L. V. *In vivo* dark-field reflection-mode photoacoustic microscopy. *Optics Letters* **30,** 625 (2005).

141. Yao, J. & Wang, L. V. Sensitivity of photoacoustic microscopy. *Photoacoustics* **2,** 87–101 (2014).

142. Yang, X., Jiang, B., Song, X., Wei, J. & Luo, Q. Fast axial-scanning photoacoustic microscopy using tunable acoustic gradient lens. *Optics Express* **25,** 7349 (2017).

143. Jiang, M., Zhang, X., Puliafito, C. A., Zhang, H. F. & Jiao, S. Adaptive optics photoacoustic microscopy. *Optics Express* **18,** 21770 (2010).

144. Cox, B., Laufer, J. G., Arridge, S. R. & Beard, P. C. Quantitative spectroscopic photoacoustic imaging: a review. *Journal of Biomedical Optics* **17,** 061202 (2012).

145. Wen, G. & Wang, L. Quantitative photoacoustic measurement of absolute oxygen saturation in deep tissue (Conference Presentation). in *Photons Plus Ultrasound: Imaging and Sensing 2018* **10494,** 104941B (International Society for Optics and Photonics, 2018).

Vita

Hsun-Chia Hsu

EDUCATION

California Institute of Technology (Caltech)

Ph.D. visiting student | Medical Engineering Sept. 2017 – Present

Washington University in St. Louis (WUSTL)

Ph.D. candidate | Biomedical Engineering Sept. 2013 – Present

National Taiwan University (NTU) – Molecular Imaging Center (MIC)

Research Assistant Sept. 2011 – Jul. 2013

National Taiwan University

M.S. | Physics Sept. 2007 – Feb. 2010

National Taiwan University

B.S. | Physics Sept. 2003 – Aug. 2007

REFEREED JOURNAL PUBLICATIONS

1. **Hsun-Chia Hsu**, Lei Li, Junjie Yao, Terence T. W. Wong, Junhui Shi, Ruimin Chen, Qifa Zhou, and Lihong V. Wang, "Dual-axis illumination for virtually augmenting the detection view of optical-resolution photoacoustic microscopy," *J. Biomed. Opt*. (accepted).
2. **Hsun-Chia Hsu***, Andria L. Ford*, Stephen Rogers, Toru Imai, Konstantin Maslov, Allan Doctor, Jin-Moo Lee, and Lihong V. Wang, "In vivo optical-resolution photoacoustic microscopy of sickle cell disease on in humans," (manuscript in preparation).
3. Wen Bao, Terence T. W. Wong, **Hsun-Chia Hsu,** Yuecheng Shen, and Lihong V. Wang, "High-speed acoustic feedback based adaptive optics photoacoustic microscopy for microvascular imaging in vivo," (manuscript in preparation).
4. Yang Li, Terence T. W. Wong, Junhui Shi, **Hsun-Chia Hsu**, and Lihong V. Wang,"Multifocal photoacoustic microscopy using a single-element ultrasonic transducer through an ergodic relay," (manuscript in preparation).
5. Terence T. W. Wong, Ruiying Zhang, Chi Zhang, **Hsun-Chia Hsu**, Konstantin I. Maslov, Lidai Wang, Junhui Shi, Ruimin Chen, K. Kirk Shung, Qifa Zhou, and Lihong V. Wang, "Label-free automated three-

dimensional imaging of whole organs by microtomy-assisted photoacoustic microscopy," Nat. Commun. 8(1), 1386 (2017).

6. **Hsun-Chia Hsu**, Lidai Wang, and Lihong V. Wang, "In vivo photoacoustic microscopy of human cuticle microvasculature with single-cell resolution," J. Biomed. Opt. 21(5), 0056004 (2016).
7. Yu-Cheng Chen, **Hsun-Chia Hsu**, Chien-Ming Lee, and Chi-Kuang Sun, "Third-harmonic generation susceptibility spectroscopy in free fatty acids," J. Biomed. Opt. 20 (9), 095013 (2015).
8. Wei-Cheng Kuo, Yuan-Ta Shih, **Hsun-Chia Hsu**, Yu-Hsiang Cheng, Yi-Hua Liao, and Chi-Kuang Sun, "Virtual spatial overlap modulation microscopy for resolution improvement," Opt. Express 21(24), 30007 (2013).
9. **Hsun-Chia Hsu***, Te-Yu Tseng*, Chiu-Sheng Yang, Tsung-Hua Tsai, and Chen-Yuan Dong, "Investigation of transport dynamics in oleic acid–induced transdermal drug delivery by two-photon fluorescence microscopy: an ex-vivo study of mouse skin," J. Biomed. Opt. 18 (9), 096016 (2013).

CONFERENCE ABSTRACTS/PROCEEDINGS

1. **Hsun-Chia Hsu**, Lei Li, Junjie Yao, Terence T. W. Wong, Junhui Shi, Ruimin Chen, Qifa Zhou, and Lihong V. Wang, "Virtually Augmenting the Detection View with Dual-Axis illumination in Optical-Resolution Photoacoustic Microscopy," SPIE Photonics West 2018 BiOS, San Francisco, California, U.S.A, (Feb. 2018).
2. Terence T. W. Wong, Ruiying Zhang, **Hsun-Chia Hsu**, Konstantin Maslov, Junhui Shi, Ruimin Chen, K. Kirk Shung, Qifa Zhou, and Lihong V. Wang, "Whole-organ atlas imaged by label-free high-resolution photoacoustic microscopy assisted by a microtome," SPIE Photonics West 2018 BiOS, San Francisco, California, U.S.A, (Feb. 2018).
3. Ting-Ying Yeh, Yun-Ju Liu, **Hsun-Chia Hsu**, Mei-Tzu Chiu, Yen-Yin Lin,.Ann-Shyn Chiang, and Shi-Wei Chu, "Deep Tissue Super-resolution Stimulated Emission Depletion Microscopy Based on Optical Clearing. Annual Meeting of the Physical Society (Jan. 2013).
4. **Hsun-Chia Hsu**, Sheng-Jie Lan, Yu-Hsiang Cheng, Fu-Hsiung Chang, and Chi-Kuang Sun, "Resonance Enhancement of Third Harmonic Generation in Biological Lipids," 2nd Molecular Imaging Center Symposium Taiwan (Nov. 2012).
5. Ting-Ying Yeh, Yun-Ju Liu, **Hsin-Chia Hsu**, Mei-Tzu Chiu, Yen-Yin Lin, Ann-Shyn Chiang, and Shi-Wei Chu, "Deep Tissue Super-resolution Imaging Based on Optical Clearing and Stimulated Emission Depletion Microscopy," 2nd Molecular Imaging Center Symposium, Taiwan (Nov. 2012).
6. Sin-You Chou, **Hsun-Chia Hsu**, Szu-Yu Chen, Yi-Hua Liao, Pei-Hsun Wang, and Chi-Kuang Sun, "In vivo Harmonic Generation Biopsy for Quantitative Evaluation in Chronological Aged Skin Keratinocytes," 1st Molecular Imaging Center Symposium, Taiwan (Nov. 2011).

PROFESSIONAL ACTIVITY

Reviewer for *Journal of Biomedical Optics.*